Chapter VIII

CHAPTER VIII

SYNTHESIS AND CHARACTERIZATION OF METAL COMPLEXES WITH GUANIDINIUM-1- NAPHTHOATE AND ITS CATALYTIC APPLICATIONS IN HYDROGEN EVOLUTION REACTION AND WASTEWATER TREATMENT

8.1 INTRODUCTION

Guanidine is an organic solvent and is considered a strong base; it is the nitrogenous analog of carbonic acid. It will combine with 1-naphthoic acid to produce ligands and form metal complexes with metal ions like Mn^{2+}, Co^{2+}, Ni^{2+}, Cu^{2+}, Zn^{2+}, Cd^{2+}, Mg^{2+}, Ca^{2+}, Sr^{2+}, and Ba^{2+}. They were characterized by elemental analysis, IR, UV-visible, thermogravimetry, and powder XRD techniques. The complex shows good antimicrobial, and antioxidant activity towards pathogens. The prepared complexes show catalytic activity toward HER reaction was also presented.

Hydrogen gas is a perfect, clean, and pollution-free fuel for future generations. Production of hydrogen in recent eras is mostly attained from the burning of fossil fuels. However, the main drawback of this method is the evolution of large amounts of greenhouse gases. Hydrogen production is also possible by employing electro, photo electrocatalytic, and water-splitting processes but it requires a more efficient catalyst. Noble metals like platinum, iridium, and ruthenium exhibit good catalytic activity but it is too expensive. Many metal oxide semiconductors like titanium oxide, nickel oxide, and zinc oxide were extensively used as catalysts for HER. The high band gap energy and formation of free radicals in the presence of UV light are considered the main disadvantages of these metal oxides. We found from the literature that the conversion of the dative bond to a sigma bond between metal and nitrogen atoms will increase the metal complex stability and thereby increase hydrogen evolution. Hence, it is extremely needed to synthesize simple, low-cost metal complexes as catalysts to increase the evolution of hydrogen. The present work focused on the synthesis of new transition metal complexes Co (II) Ni (II), and Cu (II)as electrocatalysts for hydrogen evolution.

Furthermore, the synthesized metal complex was annealed at 700° C to form metal oxide as a final product which was found to be an efficient inhibitor for the treatment of wastewater effluents from industries. We are also interested in synthesizing metal oxides (NiO, MnO, and $NiMnO_3$) as environmentally responsive materials for the treatment of industrial effluent containing Pb (II) ions. Therefore, utilizing 1-naphthoic acid and guanidine as bridging moieties, we formed metal and mixed metal complexes of the ions Ni (II), Mn (II), and Ni-Mn (II) in the current work. The heavy metal ions are removed from the contaminated water using the targeted metal oxide NiO, MnO, and Ni-MnO_3. The results were discussed in Chapter VIII.

8.2 EXPERIMENTAL

8.2.1. Synthesis procedure

Figure 8.1 shows the schematic representation for the preparation of the ligand in which the acid and base are mixed in a 1:2 ratio by adding 1-naphthoic acid (0.17 g, 1mmol) and guanidine (0.090 mg, 2 mmol) to the 40 ml of double distilled water and heated in a water bath to dissolve completely. The resulting solution was left undisturbed for 24 hours to attain precipitation and then washed with ethanol to remove impurities and dried. The ligand prepared in the previous step was added dropwise to 10 mL of an aqueous solution containing the Metal ions $M(NO_3)_2 .6 H_2O$ were M= Mn^{2+}, Co^{2+}, Ni^{2+}, Cu^{2+}, Zn^{2+}, Cd^{2+}, Mg^{2+}, Ca^{2+}, Sr^{2+}, and Ba^{2+} (1 mmol) with continuous stirring. After a period, the precipitate was filtered with Whatman-filter paper and quenched with Milli- Q water to remove the impurities, and kept for drying.

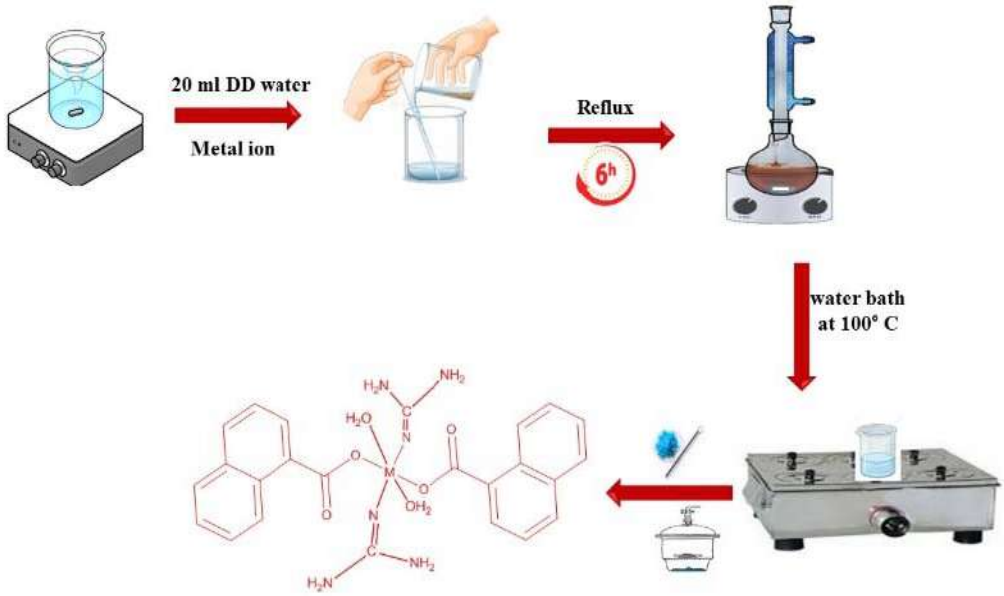

Figure 8.1 *Synthesis of metal complexes*

8.3 RESULTS AND DISCUSSION

8.3.1 Analytical Data

Elemental and analytical values of metal complexes are compared with the theoretical data which were examined in **Tables 8.1 and 8.2**. All the metal complexes imply they are stable at room temperature, decompose on heating, and are non-hygroscopic. They were not soluble in aqueous solvents but dissolved in common organic solvents.

8.3.2 FT-IR spectra

The nature of bonding with the ligand and metal ion is displayed in IR spectral studies of the solid metal complexes. The absorption peak about 1674 cm^{-1} represents the CH=N stretching frequency and a broad band at 3108 cm^{-1} is due to the stretching frequency of N-H. The strong band for C=C, C-N, and N-N epitomized around 1518,136 and 1135 cm^{-1}. In all the metal complexes the absorption band of the CH=N stretching frequency shifted to their lower frequencies towards the central metal ions which suggests the coordination mode between the nitrogen in the range from 1635-1639 cm^{-1}. In addition, the N-H group in the ligand disappeared in the metal complexes spectra which implies the linkage of the base molecule to the metal which were illustrated in Figure 8.2 and Table 8.3 1.

Table 8.1 *Analytical data*						
Metal Complexes	**Molecular weight (g/mol)**	**Color**	**pH**	**Melting point (ºC)**	**Metal (%)**	
					Found	**Calc**
[Mn $(CH_5N_3)_2$ $\{C_{10}H_7(1\text{-}COO)\}_2.2H_2O$]	549.44	Light pink	7	245	10.0	10.1
[Co $(CH_5N_3)_2$ $\{C_{10}H_7(1\text{-}COO)\}_2.2H_2O$]	553.43	Pink	6	249	10.6	10.5
[Ni $(CH_5N_3)_2$ $\{C_{10}H_7(1\text{-}COO)\}_2.2H_2O$]	553.19	Green	7	233	10.1	10.0
[Cu $(CH_5N_3)_2$ $\{C_{10}H_7(1\text{-}COO)\}_2.2H_2O$]	558.05	Blue	8	287	11.3	11.5
[Zn $(CH_5N_3)_2$ $\{C_{10}H_7(1\text{-}COO)\}_2.2H_2O$]	559.88	Duty white	8	203	11.8	11.6
[Cd $(CH_5N_3)_2$ $\{C_{10}H_7(1\text{-}COO)\}_2.2H_2O$]	606.91	white	7	259	18.2	18.0
[Ca $(CH_5N_3)_2$ $\{C_{10}H_7(1\text{-}COO)\}_2.2H_2O$]	534.58	White	7	267	10.5	10.4
[Sr $(CH_5N_3)_2$ $\{C_{10}H_7(1\text{-}COO)\}_2.2H_2O$]	582.12	White	6	287	15.0	15.4
[Ba $(CH_5N_3)_2$ $\{C_{10}H_7(1\text{-}COO)\}_2.2H_2O$]	631.83	White	6	249	21.7	20.9
[Mg $(CH_5N_3)_2$ $\{C_{10}H_7(1\text{-}COO)\}_2.2H_2O$]	518.80	White	6	269	14.6	14.5

Table 8.2 *Elemental data*				
Complexes	**% Carbon Found (Cald)**	**% Hydrogen Found (Cald)**	**% Nitrogen Found (Cald)**	**% Oxygen Found (Cald)**
[Mn $(CH_5N_3)_2$ $\{C_{10}H_7(1\text{-}COO)\}_2.2H_2O$]	51.46 (52.00)	5.77 (4.71)	15.29 (15.05)	18.37 (17.39)
[Co $(CH_5N_3)_2$ $\{C_{10}H_7(1\text{-}COO)\}_2.2H_2O$]	51.03 (52.01)	4.73 (4.70)	15.20 (15.13)	17.36 (17.31)
[Ni $(CH_5N_3)_2$ $\{C_{10}H_7(1\text{-}COO)\}_2.2H_2O$]	52.13 (52.01)	4.79 (4.69)	15.20 (15.15)	17.36 (17.30)
[Cu $(CH_5N_3)_2$ $\{C_{10}H_7(1\text{-}COO)\}_2.2H_2O$]	51.67 (51.60)	4.60 (4.69)	15.05 (15.03)	17.21 (17.19)
[Zn $(CH_5N_3)_2$ $\{C_{10}H_7(1\text{-}COO)\}_2.2H_2O$]	51.48 (51.36)	4.69 (4.65)	15.03 (15.00)	17.13 (17.01)
[Cd $(CH_5N_3)_2$ $\{C_{10}H_7(1\text{-}COO)\}_2.2H_2O$]	47.52 (47.49)	4.33 (4.30)	13.87 (13.87)	15.83 (15.80)
[Ca $(CH_5N_3)_2$ $\{C_{10}H_7(1\text{-}COO)\}_2.2H_2O$]	53.93 (53.89)	4.92 (4.89)	15.73 (15.70)	17.95 (17.92)
[Sr $(CH_5N_3)_2$ $\{C_{10}H_7(1\text{-}COO)\}_2.2H_2O$]	49.53 (49.50)	4.52 (4.49)	14.45 (14.40)	16.47 (16.40)
[Ba $(CH_5N_3)_2$ $\{C_{10}H_7(1\text{-}COO)\}_2.2H_2O$]	45.63 (45.60)	4.17 (4.13)	13.31 (13.29)	15.15 (15.16)
[Mg $(CH_5N_3)_2$ $\{C_{10}H_7(1\text{-}COO)\}_2.2H_2O$]	55.55 (55.50)	5.04 (5.03)	16.21 (16.19)	18.40 (15.49)

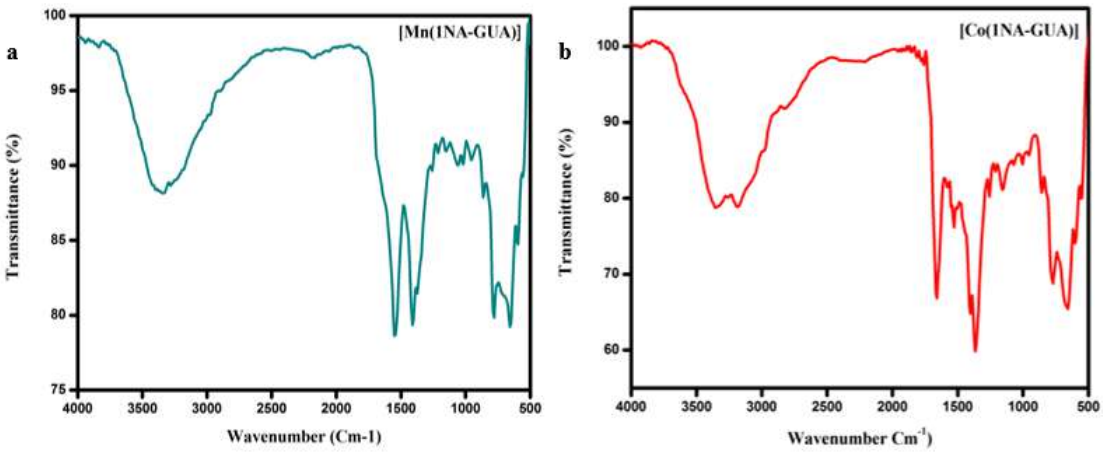

Figure 8.2 *FT-IR spectra a) Mn (II) b) Co(II) complex*

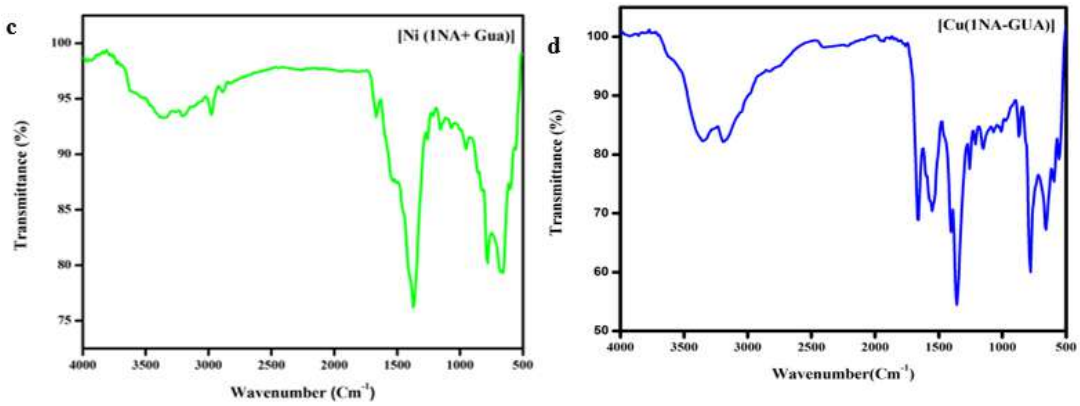

Figure 8.2 *FT-IR spectra c) Ni(II) d) Cu(II) complex*

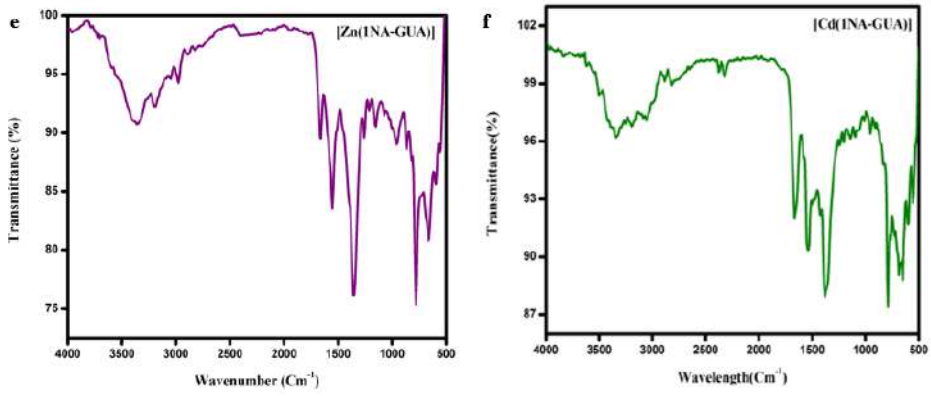

Figure 8.2 *FT-IR spectra e) Zn(II) f) Cd(II) complex*

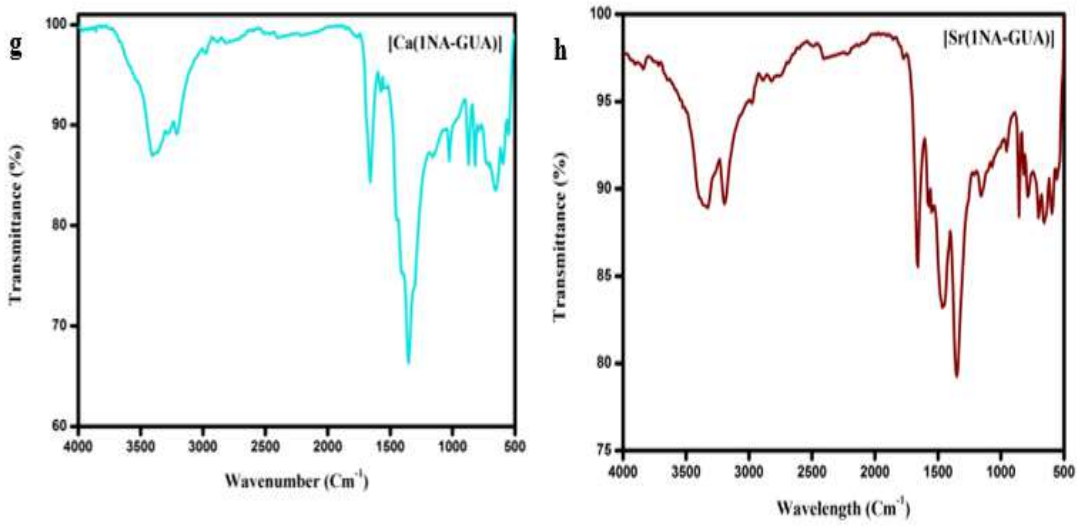

Figure 8.2 *FT-IR spectra g) Ca(II) h) Sr(II) complex*

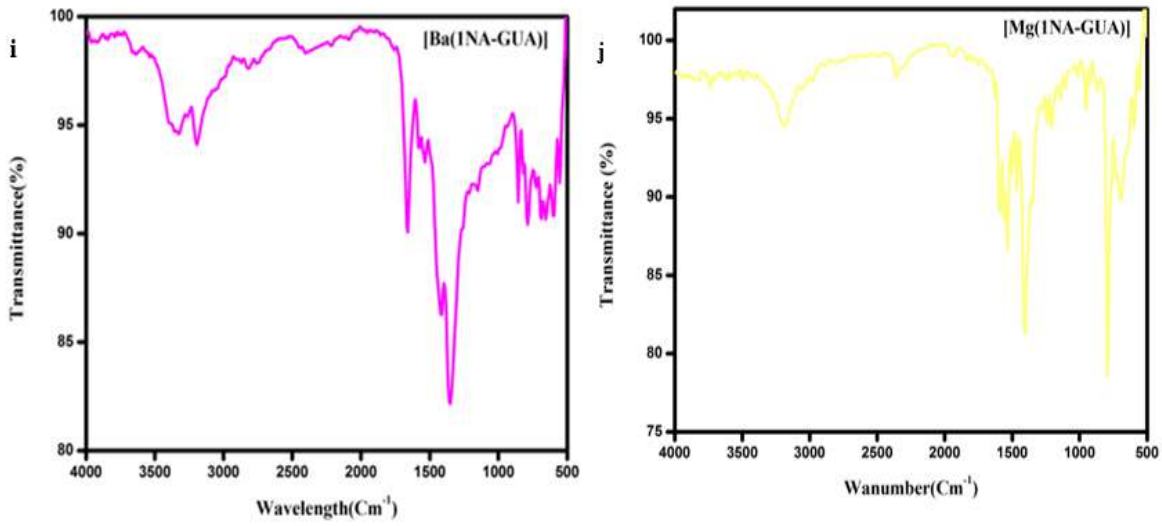

Figure 8.2 *FT-IR spectra i) Ba(II) j) Mg(II) complex*

Table 8.3 *FT-IR Spectra.*							
Complexes	**υC=N cm^{-1}**	**υC=O asym cm^{-1}**	**υC=O sym cm^{-1}**	**υ asy- υ sym cm^{-1}**	**υ M-O cm^{-1}**	**υ OH cm^{-1}**	**υ NH cm^{-1}**
[Mn $(CH_5N_3)_2$ $\{C_{10}H_7$ (1-COO)$\}_2.2H_2O$]	1221	1666	1345	321	398	3439	3358
[Co $(CH_5N_3)_2$ $\{C_{10}H_7$ (1-COO)$\}_2.2H_2O$]	1216	1663	1377	86	407	3369	3233
[Ni $(CH_5N_3)_2$ $\{C_{10}H_7$ (1-COO)$\}_2.2H_2O$]	1221	1660	1374	286	394	3424	3183
[Cu $(CH_5N_3)_2$ $\{C_{10}H_7$ (1-COO)$\}_2.2H_2O$]	1214	1655	1367	288	379	3567	3377
[Zn $(CH_5N_3)_2$ $\{C_{10}H_7$ (1-COO)$\}_2.2H_2O$]	1223	1628	1370	258	385	3435	3212
[Cd $(CH_5N_3)_2$ $\{C_{10}H_7$ (1-COO)$\}_2.2H_2O$]	1221	1668	1368	300	402	3344	3190
[Ca $(CH_5N_3)_2$ $\{C_{10}H_7$ (1-COO)$\}_2.2H_2O$]	1221	1749	1375	374	372	3380	3169
[Sr $(CH_5N_3)_2$ $\{C_{10}H_7$ (1-COO)$\}_2.2H_2O$]	1289	1631	1352	279	394	3395	3051
[Ba $(CH_5N_3)_2$ $\{C_{10}H_7$ (1-COO)$\}_2.2H_2O$]	1214	1639	1421	218	408	3519	3322
[Mg $(CH_5N_3)_2$ $\{C_{10}H_7$ (1-COO)$\}_2.2H_2O$]	1229	1653	1375	278	372	3344	3205

8.3.3 Electronic spectra

The electronic spectra for all the metal complexes were studied from 200-800 nm. The complexes were dissolved in the DMSO solution by preparing a 10^{-3} M solution at room temperature. Electronic spectra of Mn((II) ion shows weak adsorption due to the spin-forbidden transition suggesting six coordination of metal ion, which were showcased in **Figure 8.3(a-j).**

The **Figure 8.3(a'-j'),** the maximum level of the band absorption and band energies were calculated using Tauc's equation.

$$(\alpha\hbar\upsilon)^{1/n} = A(\hbar\upsilon - Eg)/1 \qquad \textbf{Eq. (8.1)}$$

According to the direct band-gap rule, $(\alpha\hbar\upsilon) = A(\hbar\upsilon - Eg)$ were plotted and then extrapolated to the axis. From the extrapolated curve, the band-gap energies for metal complexes were calculated from 3.2-4.6 eV respectively.

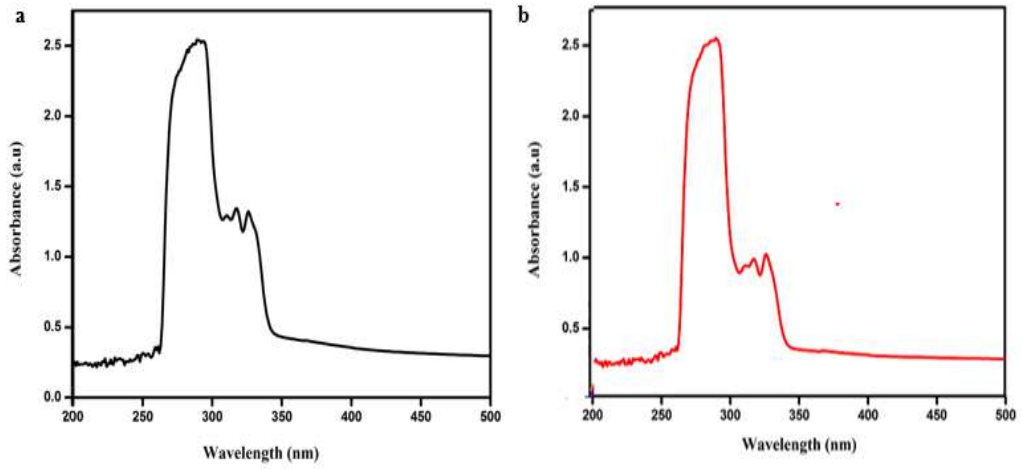

Figure 8.3 *UV-visible spectra of a) Mn (II) b) Co (II) complex*

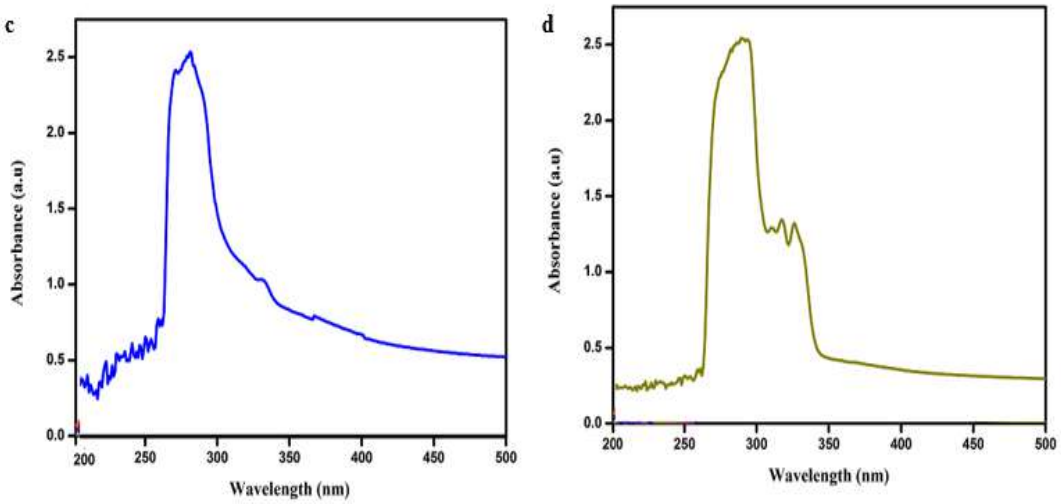

Figure 8.3 *UV-visible spectra of c) Ni (II) d) Cu (II) complex*

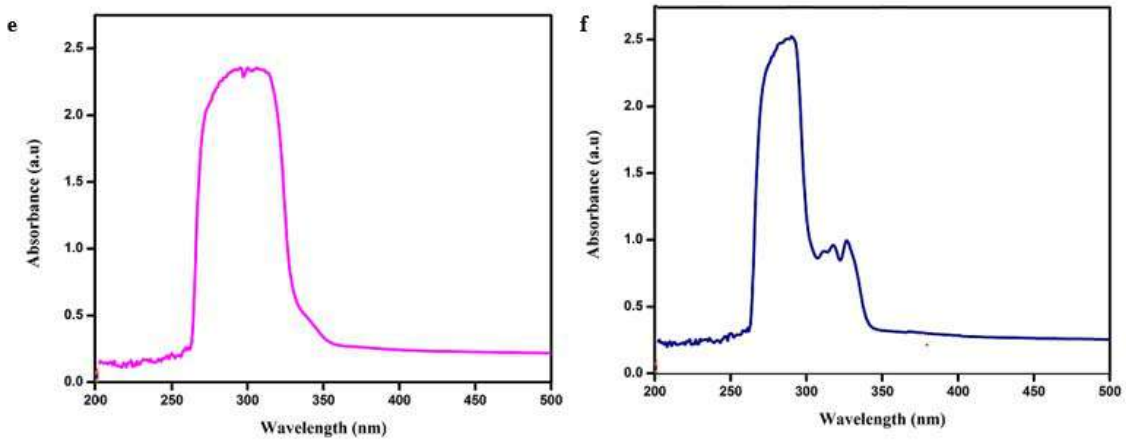

Figure 8.3 *UV-visible spectra of e) Zn (II) f) Cd (II) complex*

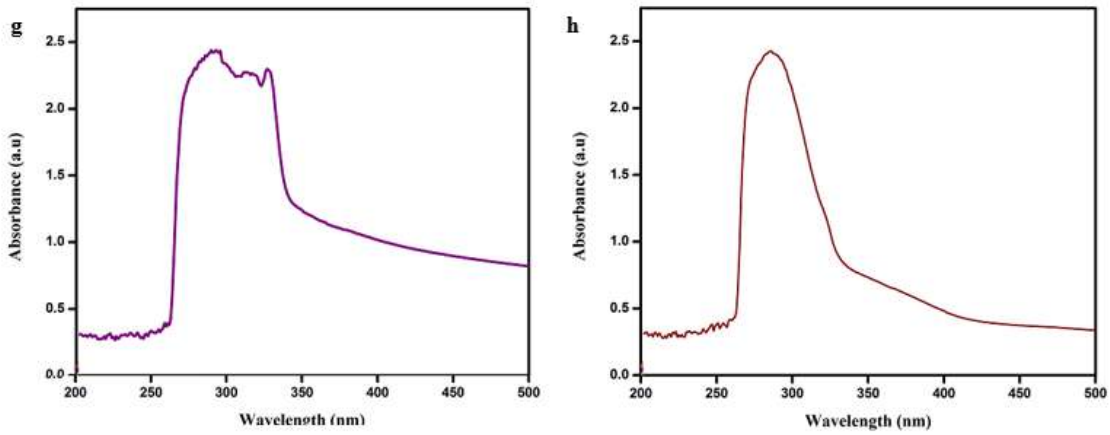

Figure 8.3 *UV-visible spectra of g) Ca (II) h) Sr (II) complex*

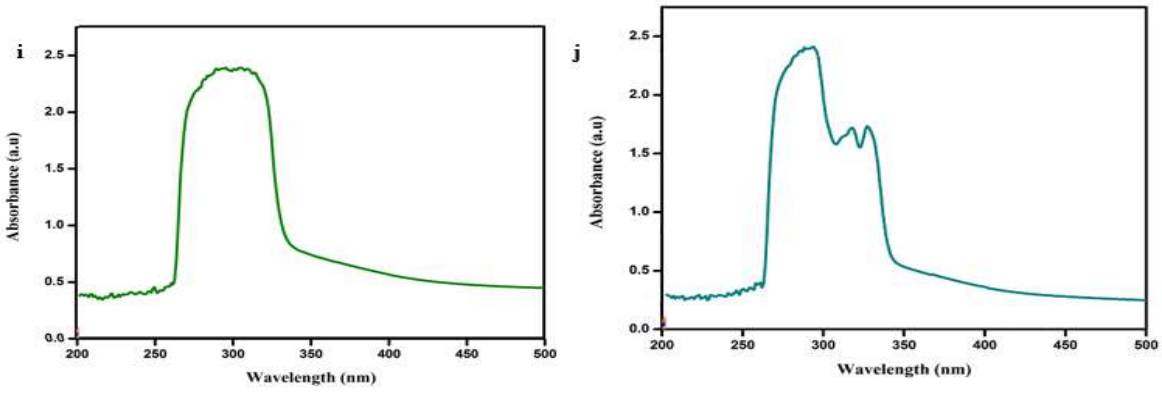

Figure 8.3 *UV-visible spectra of i) Ba (II) j) Mg (II) complex*

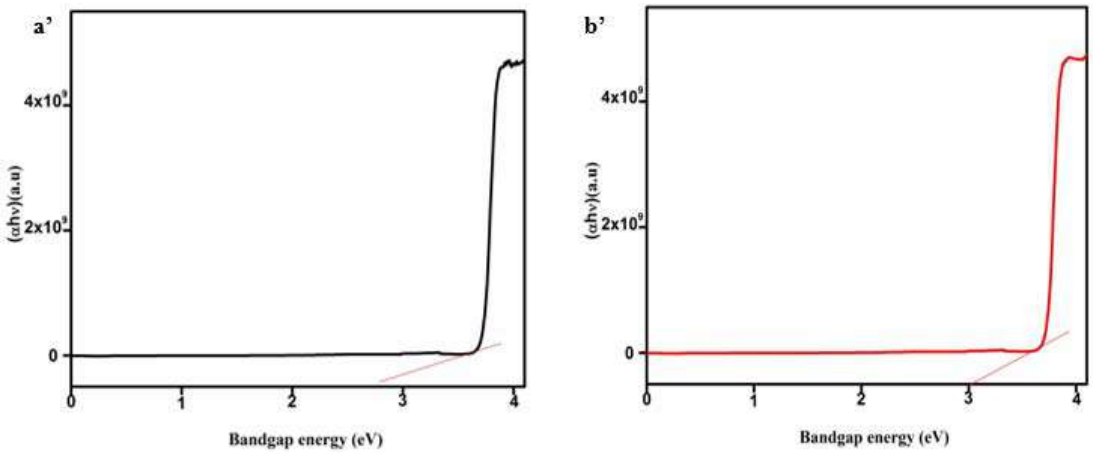

Figure 8.3 *UV-visible spectra of a') Mn (II) b') Co (II) complex*

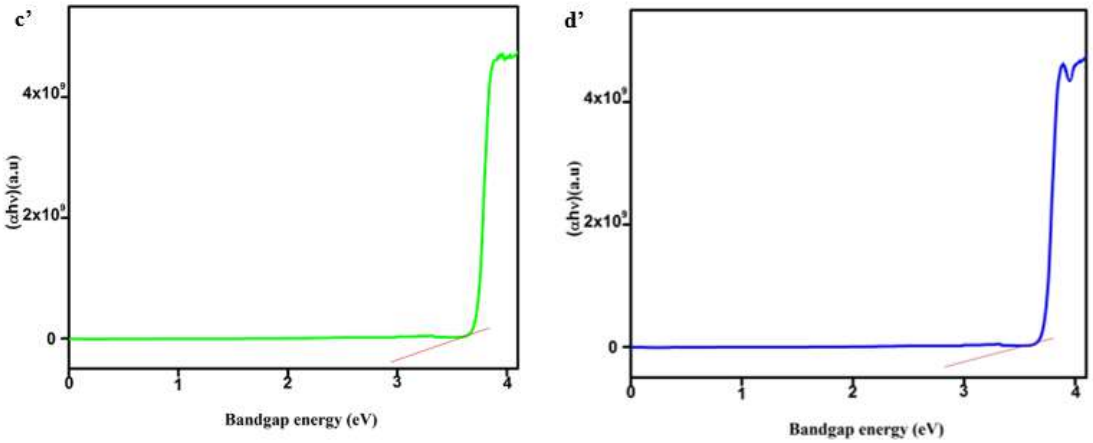

Figure 8.3 *UV-visible spectra of c') Ni (II) d') Cu (II) complex*

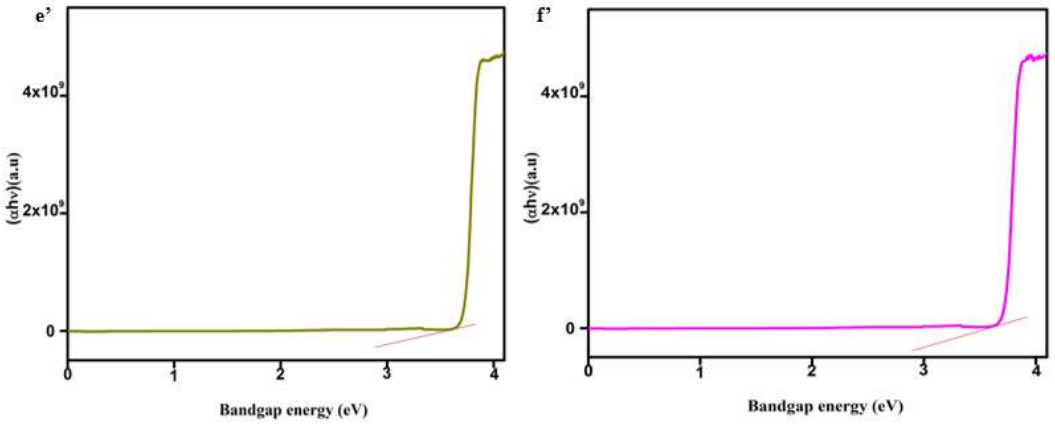

Figure 8.3 *UV-visible spectra of e') Zn (II) f') Cd (II) complex*

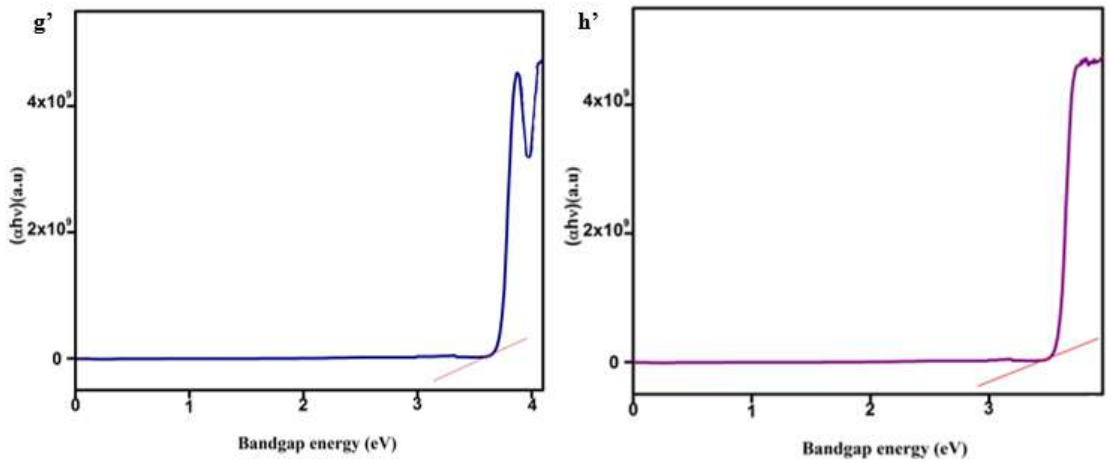

Figure 8.3 *UV-visible spectra of g') Ca (II) h') Sr (II) complex*

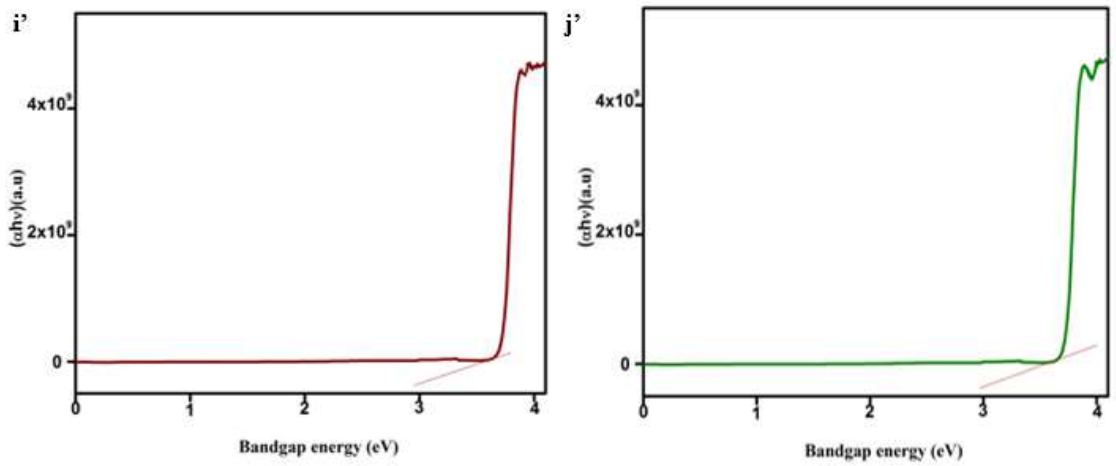

Figure 8.3 *UV-visible spectra of i') Ba (II) j') Mg (II) complex*

8.3.4 TG-DTA

The TG-DTA of the metal complexes is used to determine the position of the water molecules in the complexes and the stability of the compound. For Ni (II), Cu (II), Zn (II), and Ca (II) mass loss occurs in the first steps from 150 °C -395 °C, a second step above 396°C, and the final residue was formed in the last step (**Figure 8.4)**. For Mn (II), Co (II), Cd (II), Sr (II), Ba (II), and Mg (II) three-step decomposition process was obtained. The first phase involves the removal of water molecules at 200°C, followed by the removal of organic moiety, and finally a metal oxide is formed which is illustrated in **scheme (1)** and **Table 8.4**.

Thermal decomposition scheme (1)

$[M(CH_5N_3)_2\ \{C_{10}H_7(COO)\}_2.2H_2O]$ $\xrightarrow{150\text{-}395\ ^0C}$ $[M(CH_5N_3)_2\ \{C_{10}H_7(COO)\}_2]$ $-2H_2O$

$[M(CH_5N_3)_2\ \{C_{10}H_7(COO)\}_2]$ $\xrightarrow{396\text{-}400\ ^\circ C}$ $[M\{C_{10}H_7(COO)\}_2]$ - CH_5N_3

$[M\{C_{10}H_7(COO)\}_2]$ $\xrightarrow{400\text{-}600\ ^\circ C}$ $[MO]$

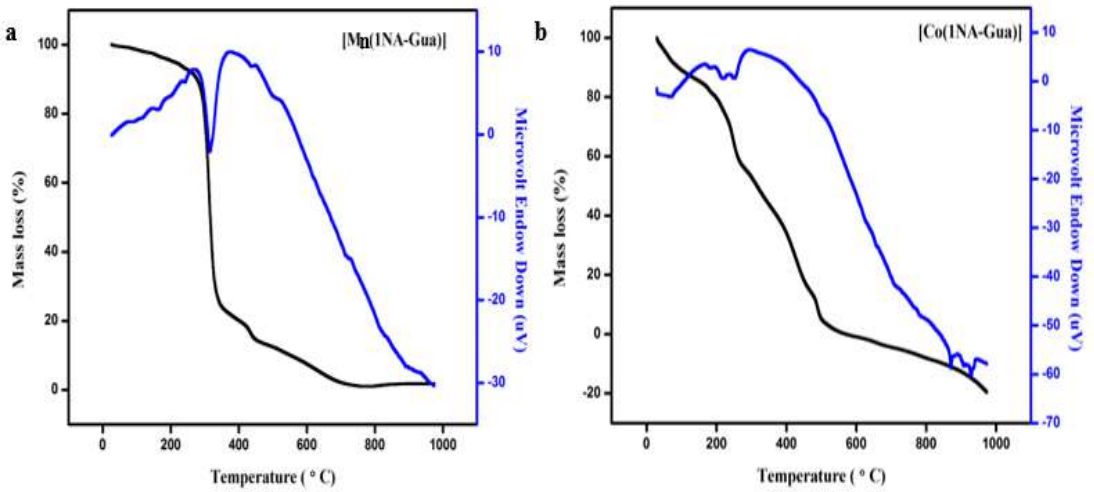

Figure 8.4 *TG-DTA a) Mn (II) b) Co(II) complex*

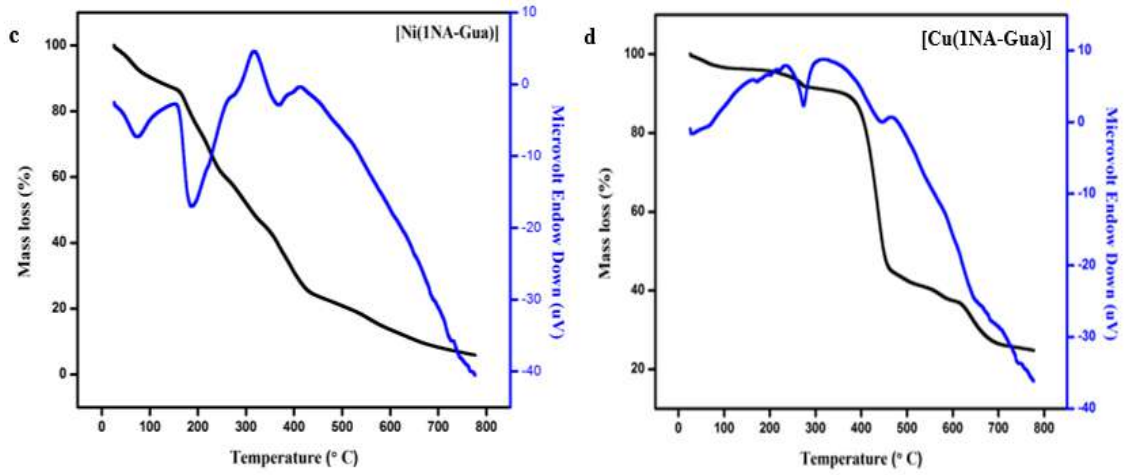

Figure 8.4 *TG-DTA c) Ni (II) d) Cu(II) complex*

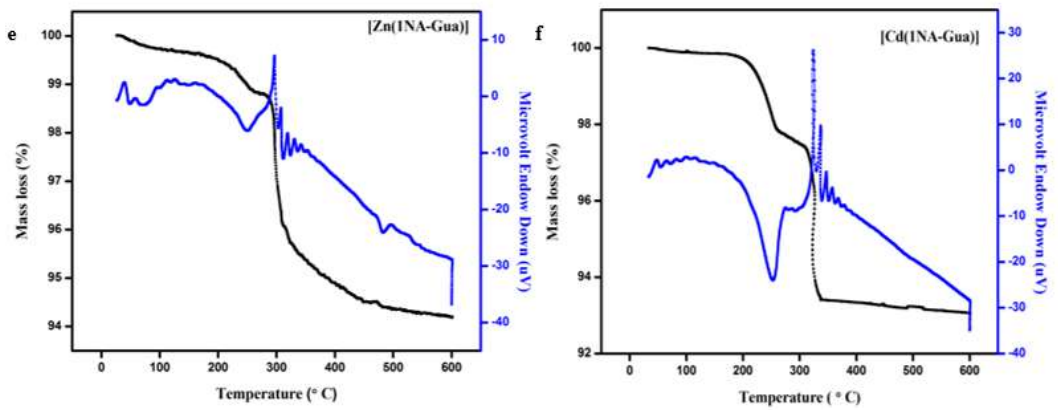

Figure 8.4 *TG-DTA e) Zn (II) f) Cd(II) complex*

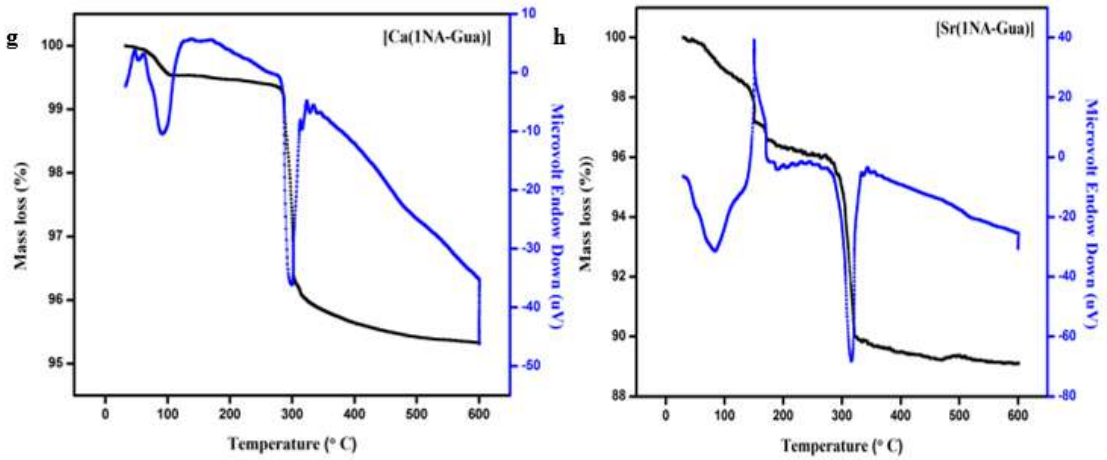

Figure 8.4 *TG-DTA g) Ca (II) h) Sr(II) complex*

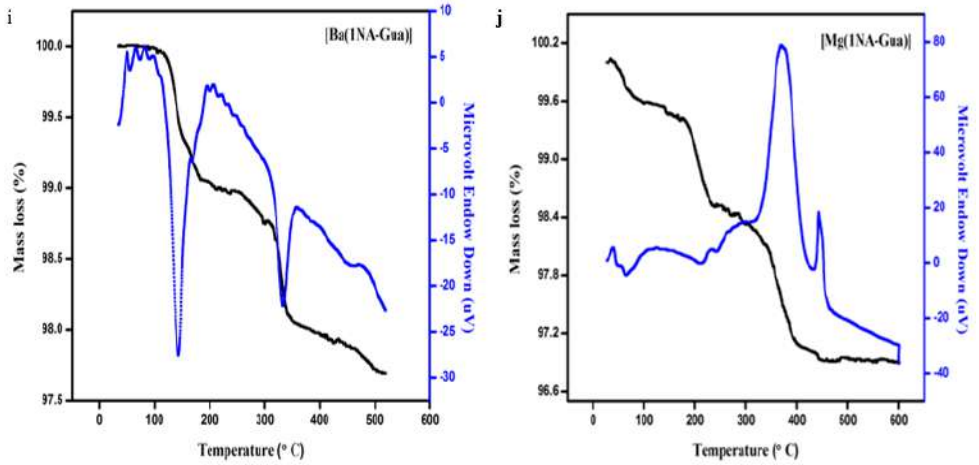

Figure 8.4 *TG-DTA i) Ba (II) j) Mg(II) complex*

Table 8.4 *Thermal Analysis*					
Molecular Formula of Complexes	**DTA Peak Temp (˚C)**	**Thermogravimetry**			**Decomposition Products**
		Temp range(˚C)	**Weight loss**		
			Observed	**Calculated**	
[Mn $(CH_5N_3)_2$ $\{C_{10}H_7$ (1-COO)$\}_2.2H_2O$]	310(-)	200-700	87.84	87.78	MnO_2
[Co $(CH_5N_3)_2$ $\{C_{10}H_7$ (1-COO)$\}_2.2H_2O$]	120(+)	80-120	6.18	5.9	[Co $(CH_5N_3)_2$ $\{C_{10}H_7(COO)\}_2.2H_2O$]
	424(+)	310-700	87.29	87.42	Co_3O_4
[Ni $(CH_5N_3)_2$ $\{C_{10}H_7$ (1-COO)$\}_2.2H_2O$]	396(-)	300-700	87.32	87.20	NiO
[Cu $(CH_5N_3)_2$ $\{C_{10}H_7$ (1-COO)$\}_2.2H_2O$]	280(-)	200-300	26.42	26.38	[Cu $(CH_5N_3)_2$ $\{C_{10}H_7(COO)\}_2.2H_2O$]
	340(-)	300-700	86.60	86.59	CuO
[Zn $(CH_5N_3)_2$ $\{C_{10}H_7$ (1-COO)$\}_2.2H_2O$]	300(-)	120-340	26.33	26.39	[Zn $(CH_5N_3)_2$ $\{C_{10}H_7(COO)\}_2.2H_2O$]
	510(-)	410-700	86.29	86.32	ZnO
[Cd $(CH_5N_3)_2$ $\{C_{10}H_7$ (1-COO)$\}_2.2H_2O$]	390(-)	250-400	24.48	24.48	[Cd $(CH_5N_3)_2$ $\{C_{10}H_7(COO)\}_2.2H_2O$]
	420(-)	400-700	79.96	80.16	CdO
[Ca $(CH_5N_3)_2$ $\{C_{10}H_7$ (1-COO)$\}_2.2H_2O$]	510	310-700	90.14	90.21	CaO
[Sr $(CH_5N_3)_2$ $\{C_{10}H_7$ (1-COO)$\}_2.2H_2O$]	300(-)	200-310	25.88	25.32	[Sr $(CH_5N_3)_2$ $\{C_{10}H_7(COO)\}_2.2H_2O$]
	400(-)	320-700	83.17	83.18	SrO
[Ba $(CH_5N_3)_2$ $\{C_{10}H_7$ (1-COO)$\}_2.2H_2O$]	430(-)	250-700	76.96	76.88	BaO
[Mg$(CH_5N_3)_2$ $\{C_{10}H_7$ (1-COO)$\}_2.2H_2O$]	350(-)	250-390	82.9	82.4	[Mg $(CH_5N_3)_2$ $\{C_{10}H_7(COO)\}_2.2H_2O$]
	485(-)	390-700	99.8	99.7	MgO

8.3.5 Powder -XRD

The growth of single crystals using solvents like ethanol, methanol, and DMF for metal complexes failed, so the synthesized complexes are characterized by powder XRD. The type of crystal system, crystalline nature, and lattice parameters were determined from XRD analysis. There is a wide difference between the XRD patterns of ligands and complexes, which reveals the formation of coordination compounds. The mean crystallite sizes of the complexes were determined. The average crystallite sizes were found to be in the range of 29-36 nm for all the complexes, as shown in **Figure 8.5,** which confirms the isomorphism among the synthesized metal complexes. The d-spacing and the relative intensities in the percentage of the diffraction patterns of all the metal complexes exhibit a similar formula, which is represented in **Table 8.5**.

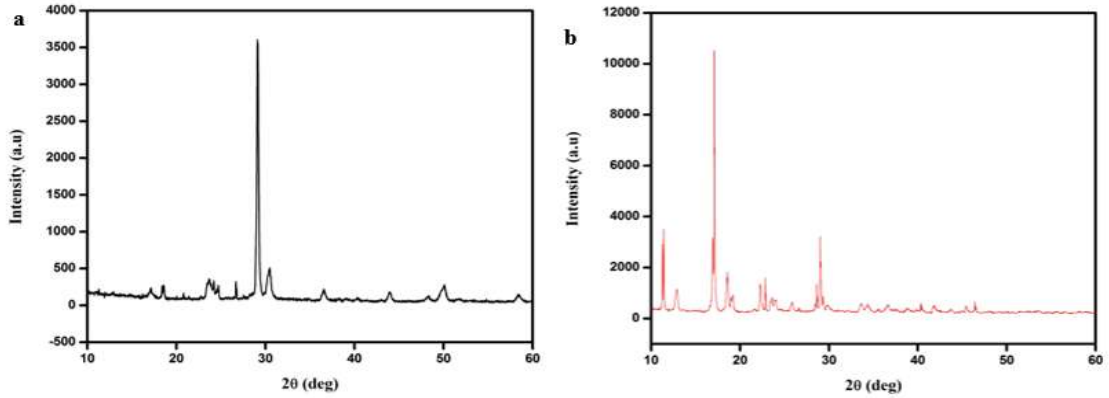

Figure 8.5 *Powder-XRD a) Mn(II) b) Co(II) complex*

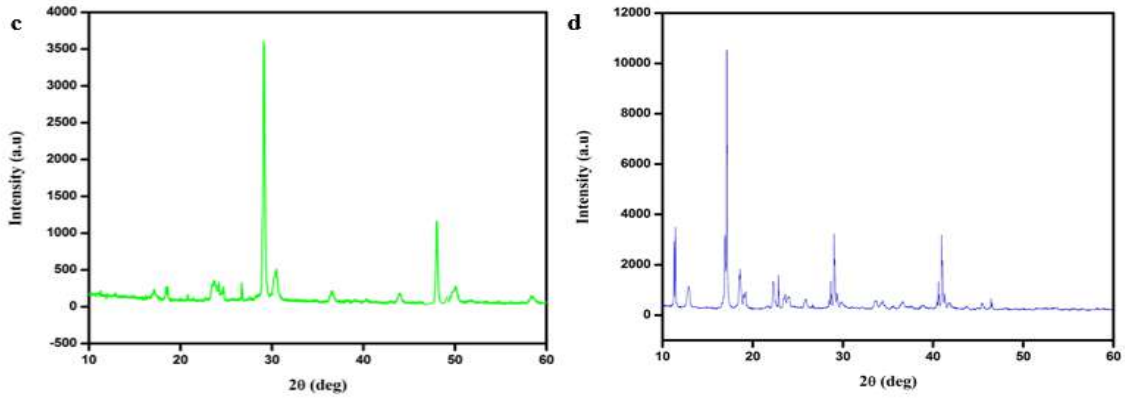

Figure 8.5 *Powder-XRD c) Ni(II) d) Cu(II) complex*

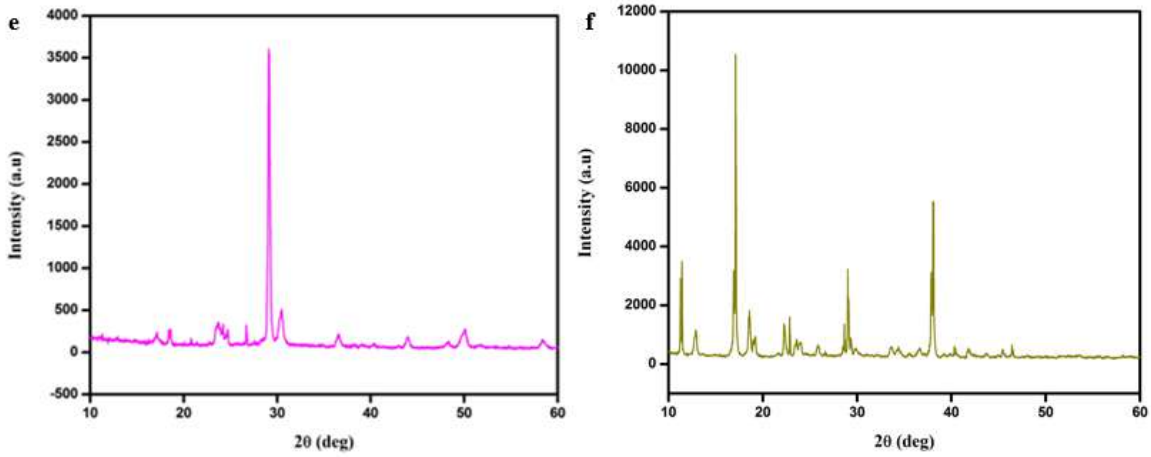

Figure 8.5 *Powder-XRD e) Zn(II) f) Cd(II) complex*

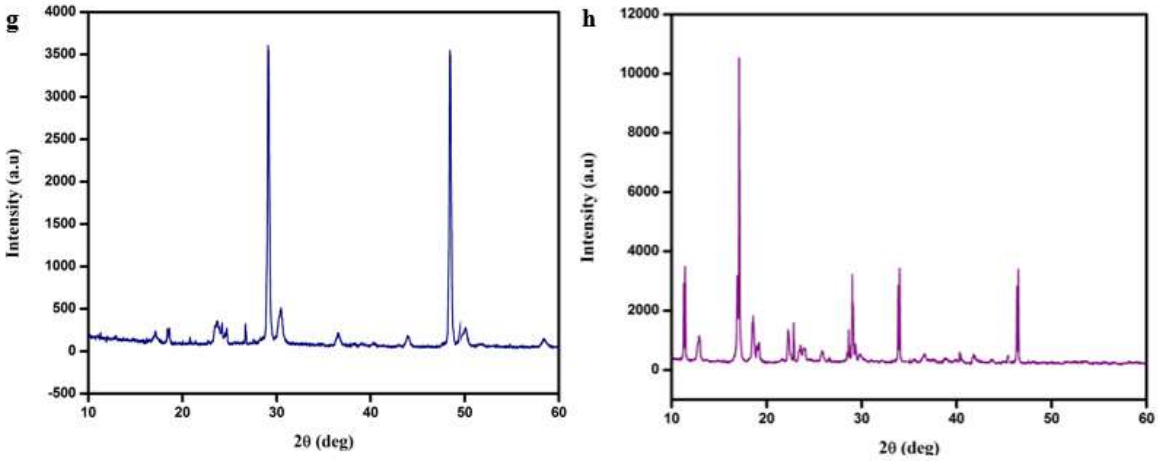

Figure 8.5 *Powder-XRD g) Ca(II) h) Sr(II) complex*

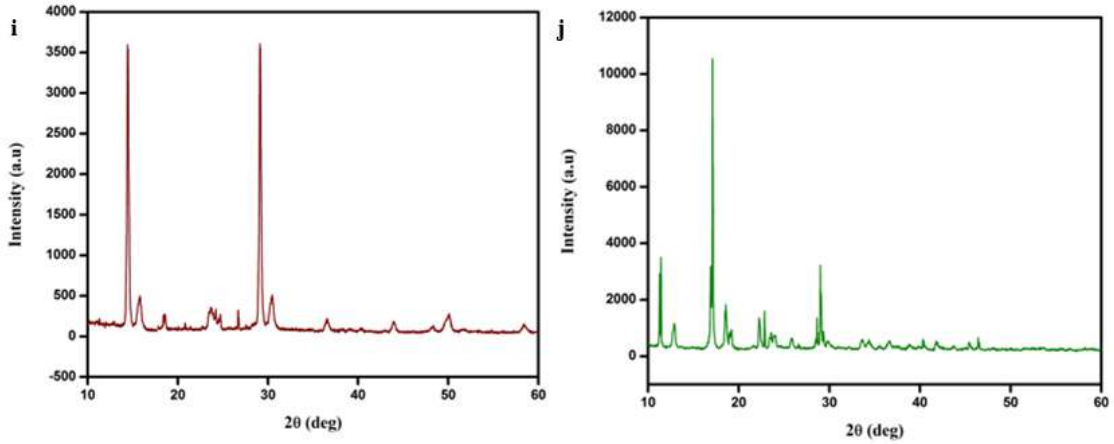

Figure 8.5 *Powder-XRD i) Ba(II) j) Mg(II) complex*

Table 8.5 *P-XRD pattern for metal complexes*							
Complex	**2θ**	**FWHM B_{size} (°)**	**D(space)**	**Complex**	**2θ**	**FWHM B_{size} (°)**	**D(space)**
[Mn ($C_2H_8N_4O_3$)$_2$ {$C_{10}H_7$(1-COO)}$_2$.2H $_2$O]	16.1	0.461	18.19	**[Cd (CH_5N_3)$_2$ {$C_{10}H_7$(1-COO)}$_2$.2H_2O]**	12.2	0.461	18.11
	19.4	0.469	17.96		16.21	0.469	17.88
	21.4	0.463	18.25		18.99	0.463	18.18
	27.2	0.502	17.02		24.76	0.502	16.94
	29.5	0.565	15.20		26.4	0.565	15.10
[Co ($C_2H_8N_4O_3$)$_2$ {$C_{10}H_7$(1-COO)}$_2$.2H $_2$O]	13.8	0.461	18.14	**[Ca (CH_5N_3)$_2$ {$C_{10}H_7$(1-COO)}$_2$.2H_2O]**	12.5	0.461	18.12
	19.0	0.469	17.95		16.5	0.469	17.89
	22.4	0.463	18.29		19.4	0.463	18.20
	27.7	0.502	17.04		25.0	0.502	16.94
	31.0	0.565	15.25		26.4	0.565	15.10
[Ni ($C_2H_8N_4O_3$)$_2$ {$C_{10}H_7$(1-COO)}$_2$.2H $_2$O]	12.6	0.461	18.12	**[Sr (CH_5N_3)$_2$ {$C_{10}H_7$(1-COO)}$_2$.2H_2O]**	12.5	0.461	18.12
	16.4	0.469	17.89		16.1	0.469	17.88
	18.8	0.463	18.18		19.2	0.463	18.19
	23.2	0.502	16.89		24.7	0.502	16.94
	26.5	0.565	15.10		26.7	0.565	15.11
[Cu ($C_2H_8N_4O_3$)$_2$ {$C_{10}H_7$(1-COO)}$_2$.2H $_2$O]	12.0	0.461	18.11	**[Ba (CH_5N_3)$_2$ {$C_{10}H_7$(1-COO)}$_2$.2H_2O]**	12.5	0.461	18.12
	16.0	0.469	17.88		16.1	0.469	17.88
	19.0	0.463	18.19		19.2	0.463	18.19
	21.8	0.502	16.85		24.7	0.502	16.94
	27.0	0.565	15.12		26.7	0.565	15.11
[Zn ($C_2H_8N_4O_3$)$_2$ {$C_{10}H_7$(1-COO)}$_2$.2H $_2$O]	12.5	0.461	18.12	**[Mg (CH_5N_3)$_2$ {$C_{10}H_7$(1-COO)}$_2$.2H_2O]**	12.82	0.461	18.13
	16.1	0.469	17.88		16.1	0.469	17.88
	19.2	0.463	18.19		18.88	0.463	18.18
	23.4	0.502	16.89		24.86	0.502	16.94
	26.6	0.565	15.10		26.71	0.565	15.11

8.3.6 Antimicrobial activity towards metal complexes

The antimicrobial activity of complexes Ni (II), Co (II), Cu (II), and Zn (II) is to detect and monitor the inhibition growth of microbes such as *Staphylococcus aureus, and Escherichia coli*. and *Aspergillus fumigates*. Our experiment reveals that Cu (II) metal complexes illustrate better antimicrobial activity against *Escherichia coli* than the other microbes. The detailed data on the antimicrobial properties of complexes have been incorporated in **Table**. **8.6,8.7**. Through this method, it has been detected that Cu (II) complexes are more efficiently active toward antimicrobials, as shown in **(Figures 8.6,8.7)**. Due to the coordination of hetero-atoms with the metal ions, there is a change in the dipole moment; hence, these metal complexes show a greater tendency towards a biomolecular interaction. The polarity change in metal complexes might be the cause of improved antimicrobial activity and interactions with the cell membrane of the strains examined in **Figure 8.8 (a, b)**.

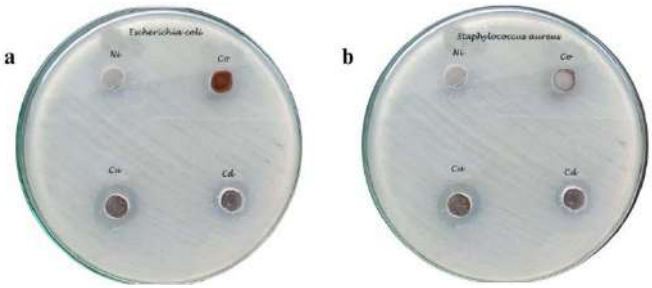

Figure 8.6 *Antimicrobial activity of Cu (II) complex against a) Staphylococcus aureus b) Escherichia coli*

Figure 8.7 *Antifungal activity of Cu (II) complex against Aspergillus fumigates*

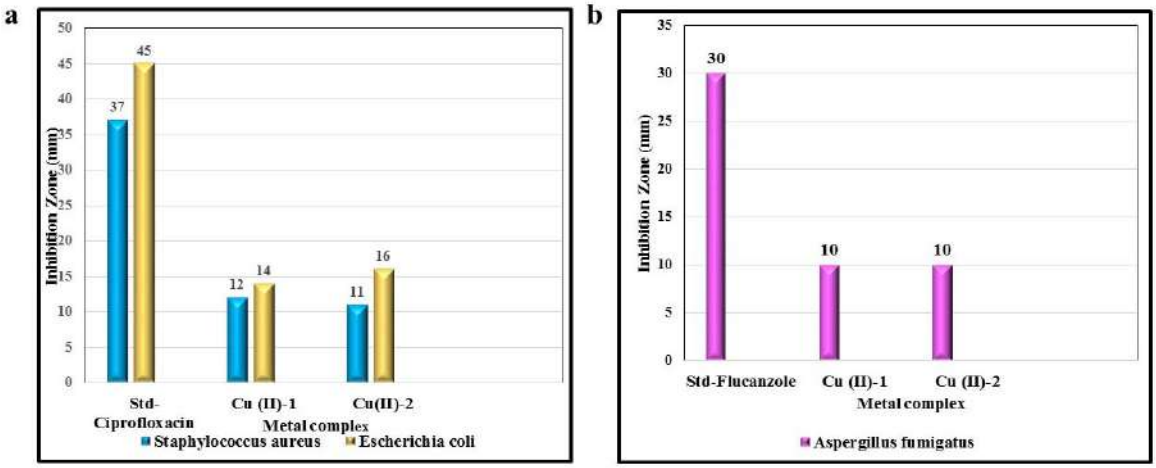

Figure 8.8 *Inhibition evaluation of the Cu (II) complex against a) Bacteria b) Fungal*

Table 8.6 *Antibacterial activity*		
Compound	**Inhibition zone (mm) (100µg/disc)**	
	Staphylococcus aureus	***Escherichia coli***
Standard – Ciprofloxacin	37	45
Cu (II)-1	12	14
Cu (II)-2	11	16

Table 8.7 *Antifungal activity*	
Compound	**Inhibition zone (mm) (100µg/disc)** ***Aspergillus fumigates***
Standard – Fluconazole	30
CuO (1)	10
CuO (2)	10

8.3.7 *Anti-Oxidant activity*

The antioxidant activity of Cu (II) is estimated by using the scavenging of the DPPH (2, 2′ -diphenyl-1-picryl hydroxyl) radical. The scavenging measurements of DPPH• were determined spectrophotometrically. DPPH was prepared in methanol, and 1 ml of DPPH methanol solution was mixed with different concentrations of 30,60,90,120,150 µg/ml. The reaction was set aside in the dark for 30 min. The reduction of DPPH• was observed by a decrease in absorbance with solvent and DPPH as blank. The percentage inhibition of DPPH activity was calculated using the following method.

$$Inhibition\ of\ DPPH\ activity\ (\%) = \frac{A_{control} - A_{sample}}{A_{control}} X\ 100 \qquad \textbf{Eq. (8.2)}$$

Where $A_{control}$ = absorbance of DPPH• in methanol without an antioxidant,

A_{sample} = absorbance of DPPH• in the presence of an antioxidant

Table 8.8. illustrates the antioxidant activity of the compound. From the experimental outcomes, enhanced antioxidant activity is detected at a concentration of 150, which shows good inhibition. **(Figure 8.9)** Among all the metal complexes, Cu (II) showed more antioxidant activity.

Table 8.8 *Antioxidant Activity*

Concentration (µg/ml)	% Inhibition
30	68.85
60	77.87
90	86.89
120	93.44
150	97.54

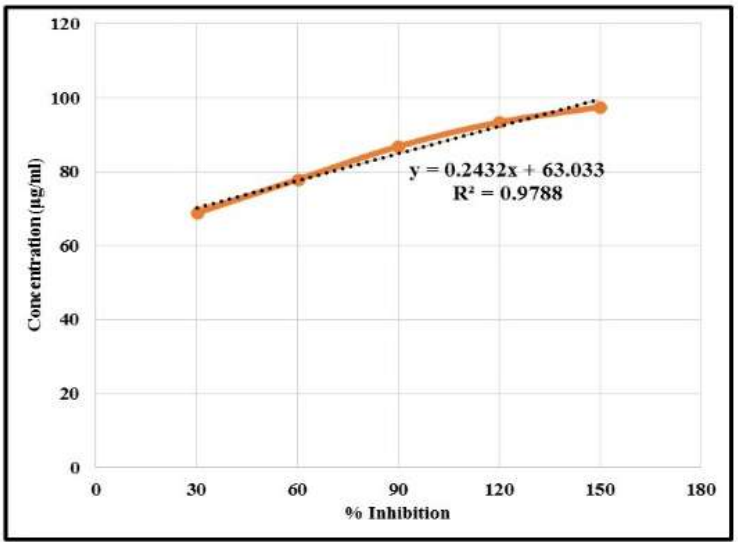

Figure 8.9 *Inhibition efficient plot of antioxidant activity*

8.4 CATALYST FOR HYDROGEN EVOLUTION REACTION

8.4.1 Cyclic voltammetry

CV experiments have been performed for the synthesized electrocatalyst in the range of -0.5 to +2.0 V vs RHE, and the voltammograms thus obtained are given in **Figure 8.10(a-c)**. In the CV curve during the 5th cycle, one current maxima is observed at 0.74V vs RHE which can be easily distinguished from the anodic part of the curve **Table 8.9**. Variations in both positions and with the intensity of the peaks may be to due incomplete reversibility. The same fact was also supported by differences in curve shape at different cycles. The area of the anodic peak was more which implies the nano-crystalline behaviour of electrocatalyst. It can be seen the electrocatalyst has more H_2 ion adsorption as well as desorption current at 0.21mM. Hence CV curves confirm that the synthesized electrocatalyst has higher cathodic current density at 0.74 V vs RHE, hence Cu^{2+} has acted as a good electrocatalyst for hydrogen evolution.

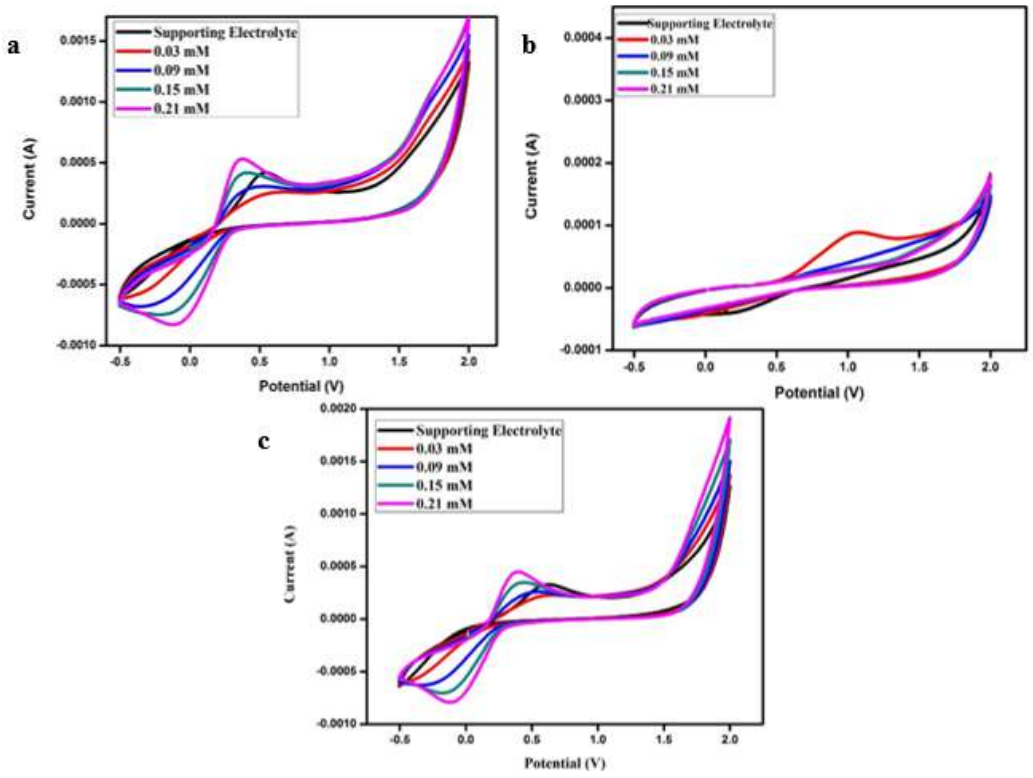

Figure 8.10 *Cyclic voltammogram a) [Ni(1NA-Gua)] b) Co (1NA-Gua)] c) Cu (1NA-Gua)]*

Table 8.9 *Current densities found from CV curves recorded at the potential range of -0.5 to 2.0 V vs. RHE*

Cycles	**Current Density at Obtained Range**		
	Ni (II)	***Co (II)***	***Cu (II)***
1st	0.67	0.22	0.68
2nd	1.01	0.38	1.02
3rd	1.05	0.47	1.06
4th	0.73	0.54	0.74
5th	0.73	0.66	0.74

8.4.2 Tafel Plot

Figure 8.11 shows a Tafel plot of the electrocatalyst with slope ranges occurring from 55-99 mV dec^{-1} implying that the hydrogen evolution reaction will follow the Volmer-Heyrosky mechanism. The slope was appreciably less than the reported one Cu^{2+}which implies that hydrogen evolution will be higher with the use of the electrocatalyst. The effect of the Cu^{2+} electrocatalyst on hydrogen evolution was measured in terms of TOF (Turnover frequency) which was found to be 27.4S^{-1}.

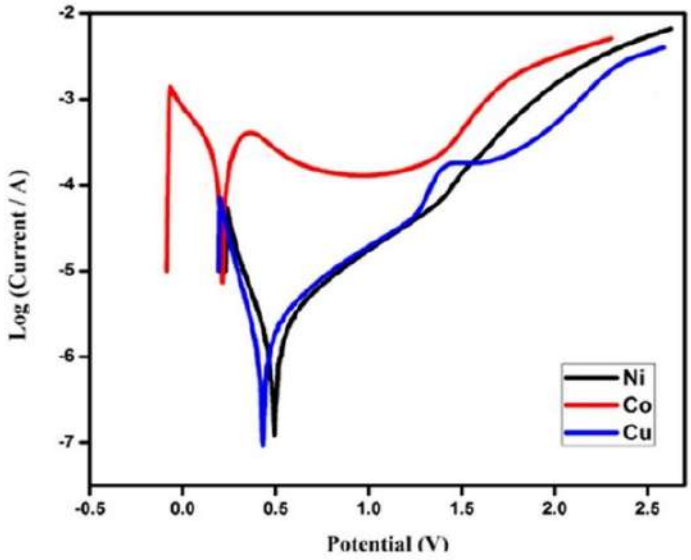

Figure 8.11 *Tafel Plot of the electrocatalyst*

8.4.3 Computational analysis (DFT)

DFT calculated the computational study for Ni (II), Co (II), and Cu (II) metal complexes. The optimized metal complexes structure runs under the Gaussian-09 software in B3LYP/6-311G (d, p). The optimized energy frames have been displayed in **Figure 8.12**. The HOMO and their LUMO band gap energy range from -0.4 to -2.1 eV due to the interaction between ligand and center metal ions. The calculated values of the HOMO–LUMO gap with the presence of the hetero atoms can be ascribed to the steadiness imparted to the LUMO and slight dislocation of the HOMO. The band gap energy implies negative values due to the metal complexes' stability. ΔE energy gap due to the transition state from HOMO→LUMO is shown in **Table 8.10**. [2]

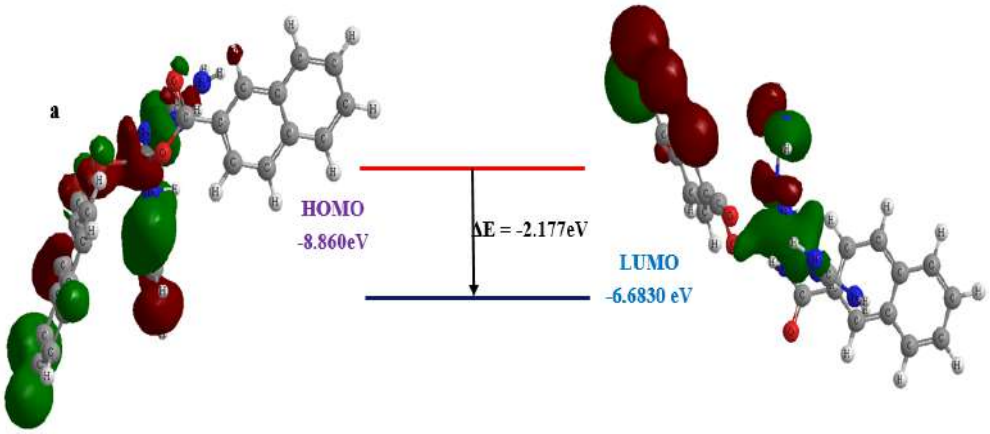

Figure 8.12 *DFT for the optimized molecular structure of a) Ni(II) complex*

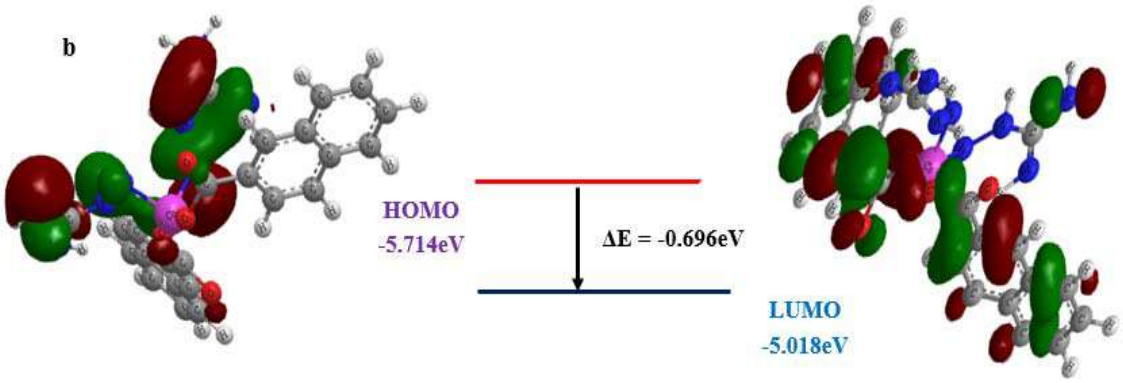

Figure 8.12 *DFT for the optimized molecular structure of b) Co(II) complex*

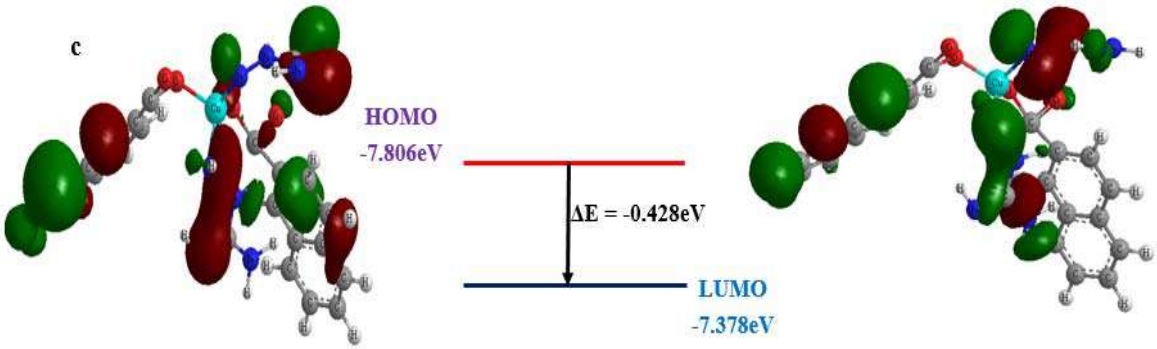

Figure 8.12 *DFT for the optimized molecular structure of c) Cu(II) complex*

Table 8.10 HOMO-LUMO levels in Electrochemical Measurement			
Compound	**HOMO**	**LUMO**	**ΔE(v)**
[Ni (1NA-GUA)]	-8.860	-6.683	-2.17
[Co (1NA-GUA)]	-5.714	-5.018	-0.69
[Cu (1NA-GUA)]	-7.806	-7.37	-0.42

8.5 ELIMINATION OF HEAVY METALS FROM INDUSTRIAL WASTEWATER

8.5.1 Water Treatment

Batch trials were led to study the impact of the metal ions on the removal capacity. Firstly, nanosized NiO, MnO, and $NiMnO_3$ (10, 25, 50, and 100 mg) were dispersed in water and sonicated for 3 hours. A stock solution of Pb (II) was processed by dissolving a known quantity of Pb $(NO_3)_2$ in 1000 mL of double distilled water. A 100 mg/L standard solution and the respective aliquots were prepared by further dilutions of the stock solution. The compound was shaken at 26 rpm chamber at room temperature and the adsorption kinetics was confirmed at 5, 10, 15, and 30, min. The liquid phase concentration was measured by the AAS instrument to detect the metal ions present in the water as illustrated in **Figure 8.13.**

8.5.2 Batch studies

The operating parameters viz., initial concentration of Pb (II), the dosage of oxides, and agitation time of sorbate-sorbent interaction were optimally validated, as they possess a significant part in the adsorption mechanism for the three systems (Pb (II) – NiO, Pb (II) – MnO & Pb (II) – $NiMnO_3$ mixture). The parametric ranges include Pb (II) initial concentration (3-12 mg/L: 3 mg/L); metal oxide dosage (10, 25, 50 & 100 mg), and time frames (5, 10, 20 & 30 mins). 50 mL of aqueous Pb(II) solutions of specified concentrations were transferred into 250 mL Erlenmeyer flasks, loaded with the metal oxides, and agitated (120 rpm) in a rotary mechanical shaker (KEMI model) at preset time intervals/1^3. The contents of the flasks were filtered and determined for the residual Pb (II)

concentrations, apart from their initial values, using Atomic Absorption Spectrophotometer (AA 6200 model, Shimadzu make) at the specific Pb (II) wavelength (283.3 nm) and slit width (0.7 nm).

8.5.3 Column Studies

Optimized conditions of a Batch method for laboratory solutions were scaled up using textile wastewater and further extended to the fixed bed column to assess the metal oxides' [4] characteristics through the continuous run of the field sample. The procedure for Mini fixed bed column packing is as follows: $NiMnO_3$ powder, that exhibited maximum Pb(II) sorption (Batch studies), was sandwiched among adjacent supporting layers of glass wool in a cylindrical glass tube (2.5 cm inner diameter and 30 cm height). The step-wise arrangement was: cotton (1 cm), glass wool layer (3 cm), glass beads (2 cm), $NiMnO_3$ (5 grams), and glass wool (1 cm) as shown in **Figure 8.13 c**. The purpose of adding glass wool and glass beads was to improve the distribution flow of the effluent sample, through the enhancement of mechanical strength. Pb(II) containing industrial wastewater was poured from the top of the packed column after serial dilutions [5] to bring down the concentration to 8 mg/L. The flow rate of the eluent was fixed as 50 mL 5 mins after trial runs. The collected samples were analyzed for the residual Pb(II) concentrations [6].

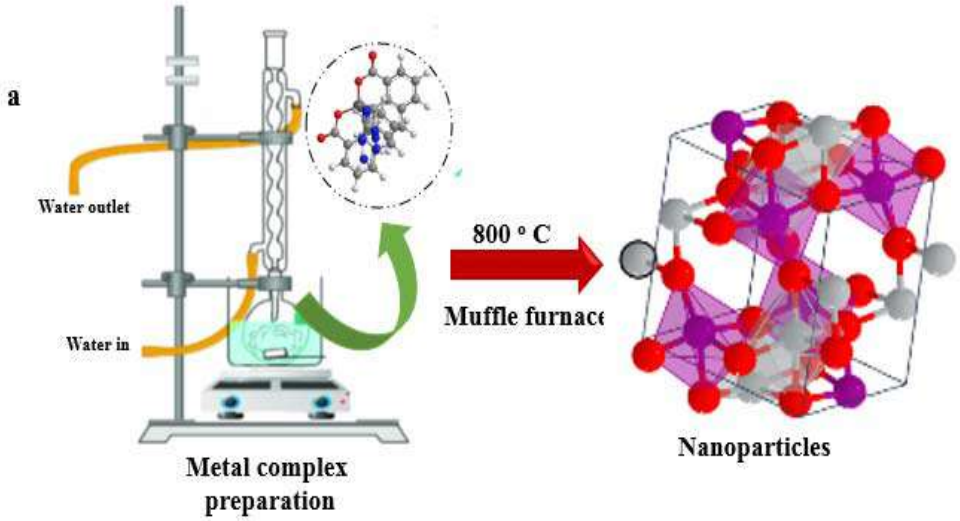

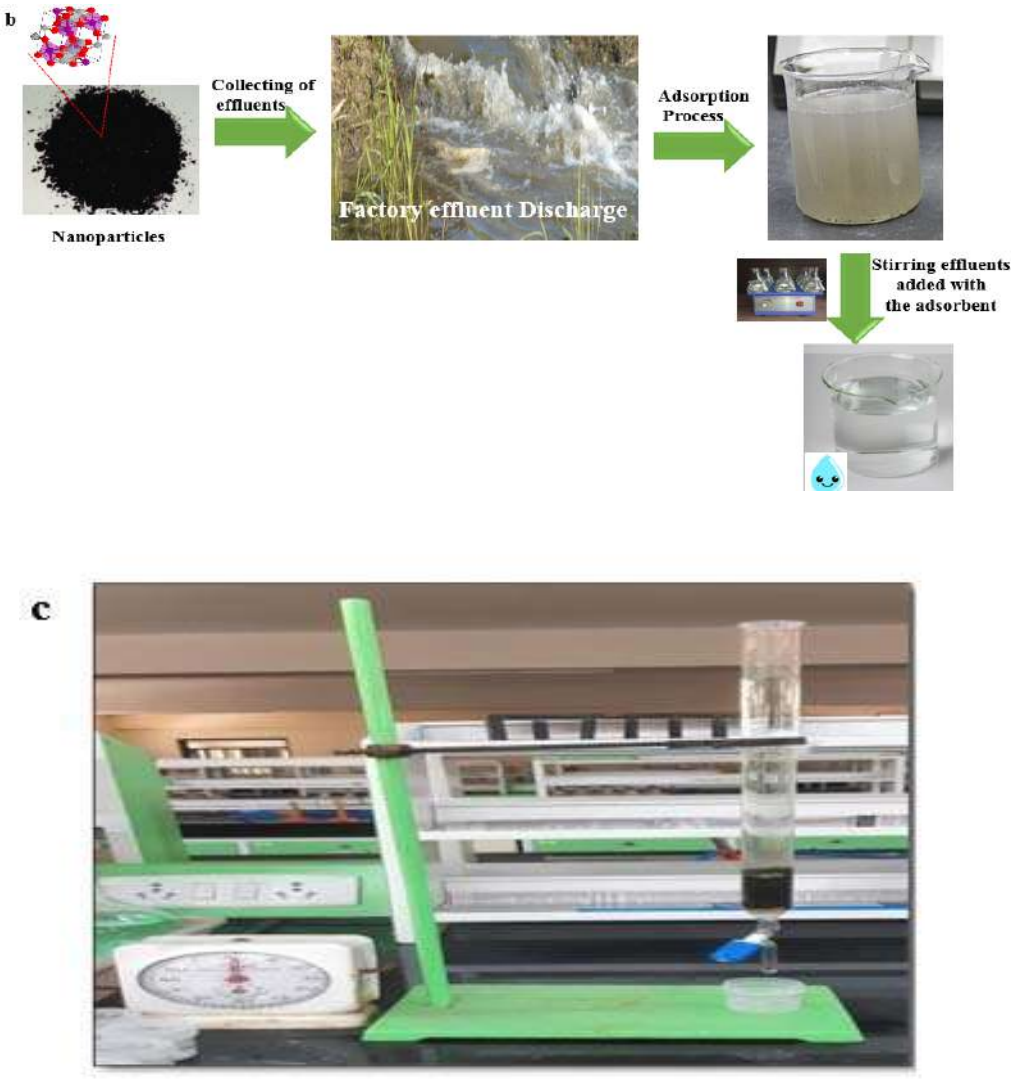

Figure 8.13 *a) Synthesis process of metal complexes b) Water treatment with nanoparticles c) Mini Fixed Bed Column.*

8.5.4 Vibrational Spectra

The NiO, MnO, and $NiMnO_3$ nanoparticles show a peak occurring at around 445-664 cm^{-1} due to the linkage between metal ions and oxygen. There is an asymmetric and symmetric stretching vibration of $-CO_2$ that occurred due to absorption from the air shown in **Figure 8.14(a-c)** [7].

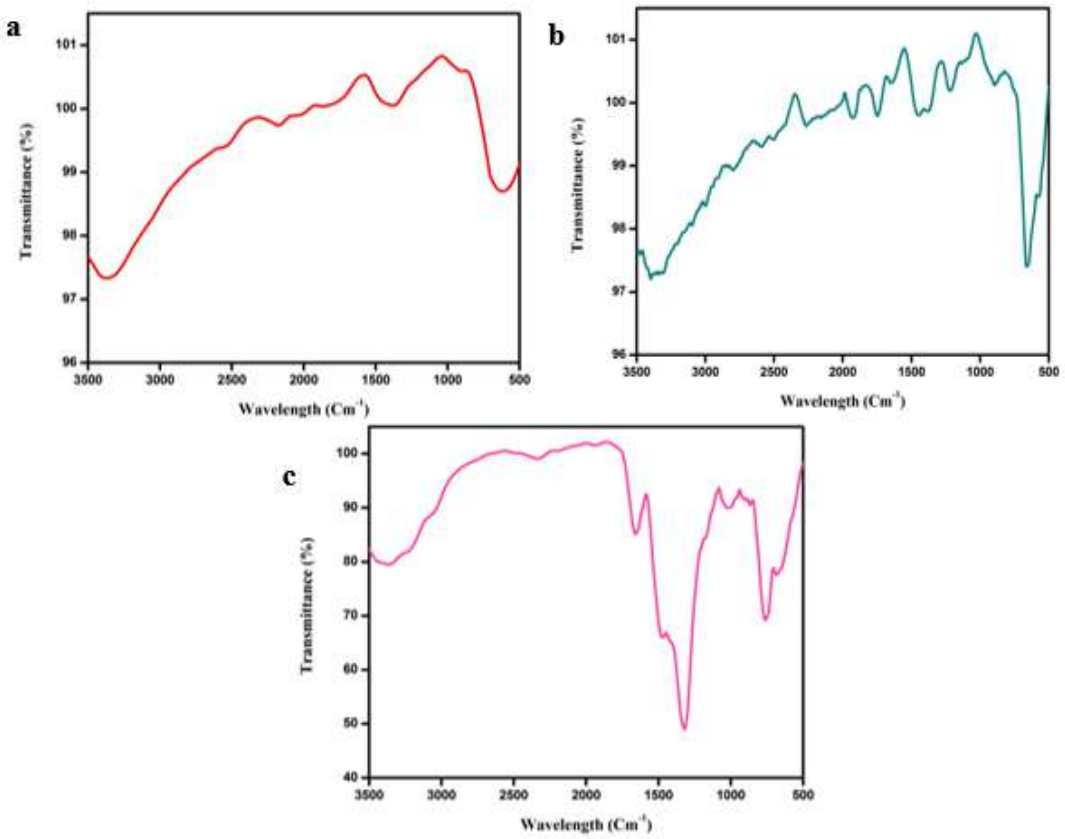

Figure 8.14 *FT-IR spectra of a) NiO b) MnO and c) $NiMnO_3$*

8.5.5 Electronic Spectra

Figure 8.15(a-b) represented the NiO, MnO, and $NiMnO_3$ nanoparticles in which the NPs band occurred at 250 nm (NiO), 284 nm (MnO), and 290 nm ($NiMnO_3$). The optical band gap (Eg) values were calculated against $(\alpha hv)^{1/2}$*vs. hv* was extrapolating against the linear line of the graph on *hv* shown in **Figure 8.16(a'-c').** The optical energy NiO, MnO, and $NiMnO_3$ NPs ranges from 4.4,4.3, and 2.5 eV whereas for complexes Ni(II), Mn(II), and mixed metal Ni-Mn arise from 3.5,3.8, and 3.9 eV [8]. The band gap energy of nano oxides will always be less than the precursor complexes owing to their small and quantum size effect.

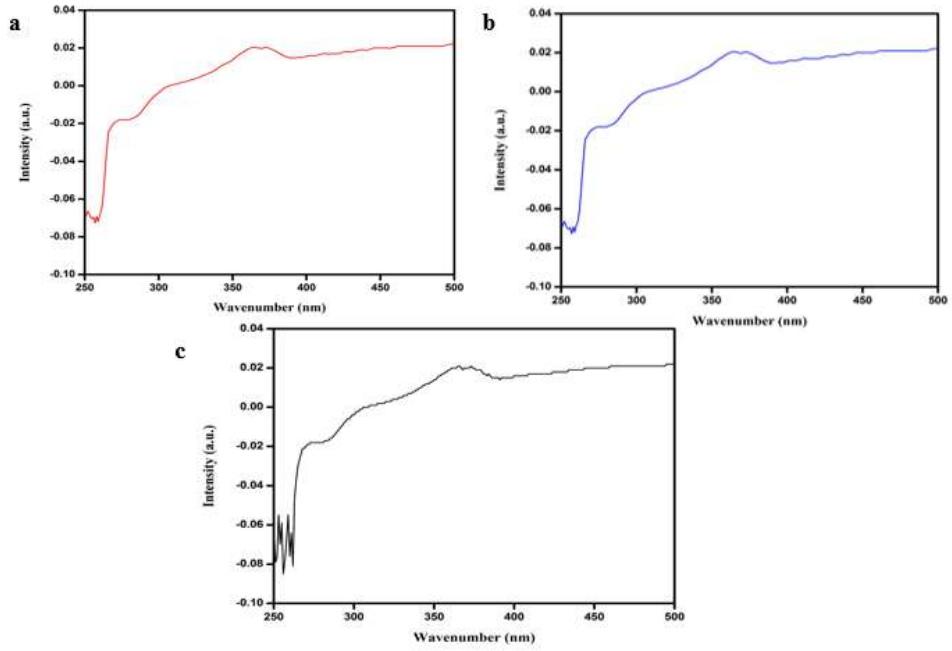

Figure 8.15 *Electronic spectra of a) NiO b) MnO and c) $NiMnO_3$*

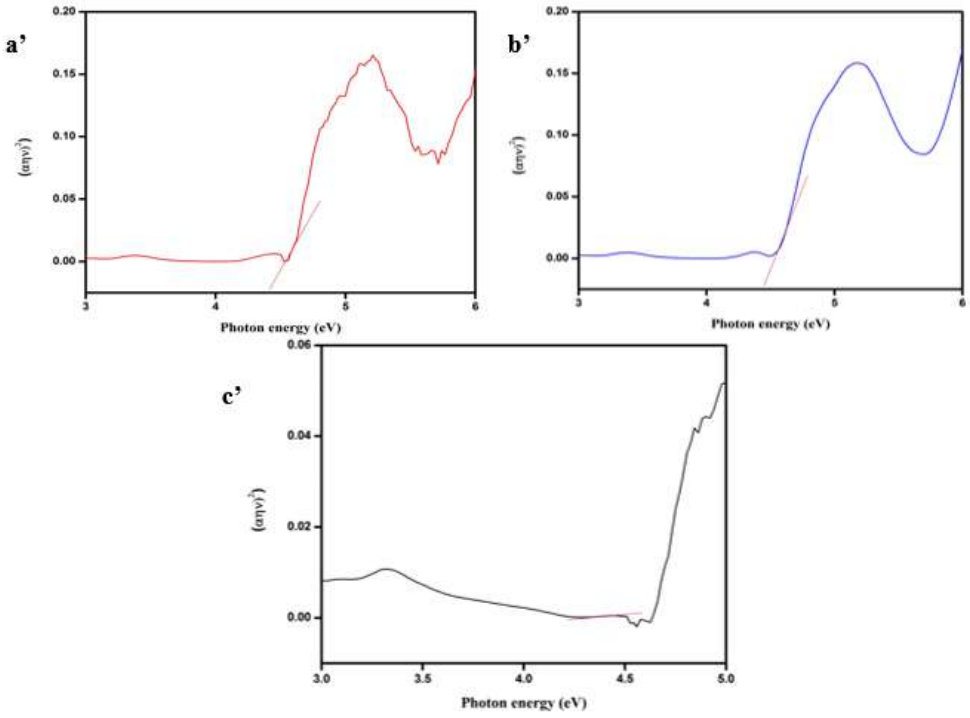

Figure 8.16 *Tauc's plot of a') NiO b') MnO and c') $NiMnO_3$*

8.5.6 DFT band structure

The DFT band structure scheming is performed to get knowledge about the physical nature of the compound. **Figure 8.17(a-c)** reveals the computed electronic band structures of NiO, MnO, and $NiMnO_3$. The Fermi levels are spotted by horizontal lines. From the GGA-PBE calculation, the valence band for NiO, MnO, and $NiMnO_3$ was determined. The 2s state of oxygen shows strong dispersive bands in the range of -4 eV in all the oxides. While the $NiMnO_3$ band occurred around 0eV, due to weak hybridization with 2p states of oxygen. The minimum conduction band was seen for both the oxides which are represented by L. Just overhead, the parabola shape signifies the strong dispersion conduction band. The bandgap E_g values, formation energy, and magnetization are shown in **Table 8.11**. The valence bands were close to the Fermi level and dragged down due to the interface between the d-state of the metal ions and the p-state of the oxygen which increases the band energy gap. The conduction band was represented by zero which shifted to the gamma points signifying the electron occupies the majority and their minority spin ensuing in zero spin moment. The theoretical DFT band gap energy was correlated with the UV-metal oxide band gap energy value obtained from experiment [9]. The moderate band gap energy of $NiMnO_3$ implies, that it requires the highest photon energy and can be used in electronic gadgets.

Partial density plots were also examined, which are shown on the right side of the band structure. For all the metal oxides, there are three major splitting of density plots; i) 2s states of oxygen atom was revealed with strong band beneath the Fermi levels around -18eV,/1ii) major involvement of 3d electrons of transition metal ions with minimal contribution from oxygen atom was seen as strong band, and iii) the vacant 3d states of metal ions with 2p hybridization of the oxygen was appeared as conduction bands [10]. In general, there is an upgradation in the 2p character of an oxygen atom and intensification in the partition amongst all the three peaks sideways of the Fermi level. The nature of the bonding between Ni, Mn, and Ni-Mn with oxygen atoms was well-established from the density distribution curve. The majority of the charges accumulate between the metal ion and O atoms due to directional bonding between both particles. It was suggested the possibility of the blended mode of the covalent and ionic bond exists between the nanoparticles owing to the low hybridization of the oxygen atom.

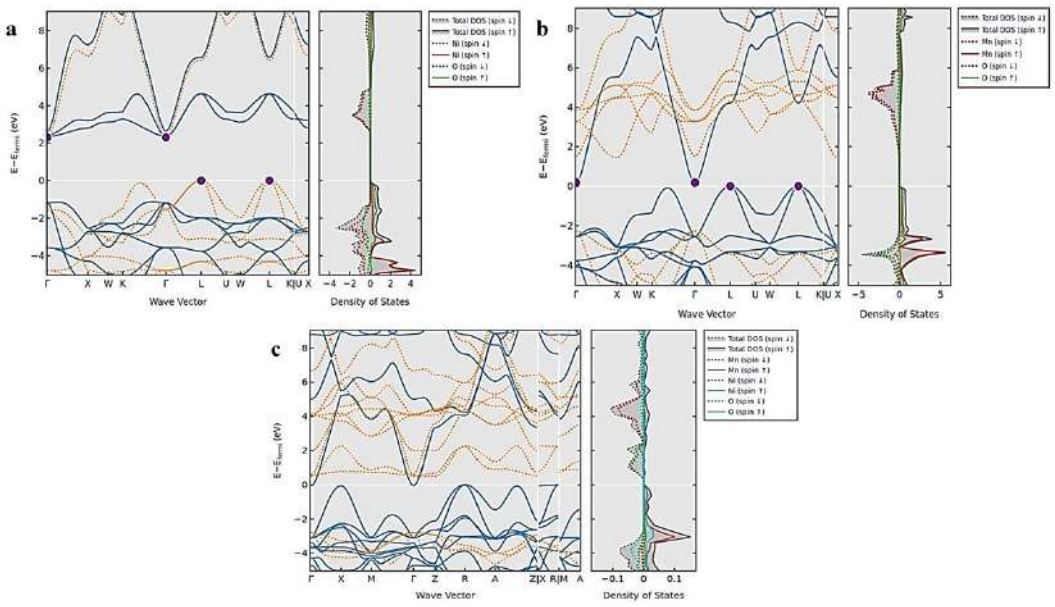

Figure 8.17 *DFT band structure a) NiO, b) MnO, and c) $NiMnO_3$.*

Table 8.11 *UV- metal oxide band gap energy value*			
Metal Oxides	**NiO**	**MnO**	**$NiMnO_3$**
Band gap (eV)	0.01	0.18	2.30
Formation energy(eV/atom)	-1.219	-1.980	-1.367
Magnetization (μB/f.u)	2.00	5.00	5.00

8.5.7 Thermal analysis

Figure 8.18 (a-c) represents the TG/DTA curves for the metal oxides in which the weight loss in TGA measurement was in good agreement with the predictable decomposition of carbon oxides. The mass loss occurred from 50-150 °C connected with the adsorbed gases on the surface of the oxides. The second weight loss was attributed to around 600 °C which is the formation of pure metal oxides [11].

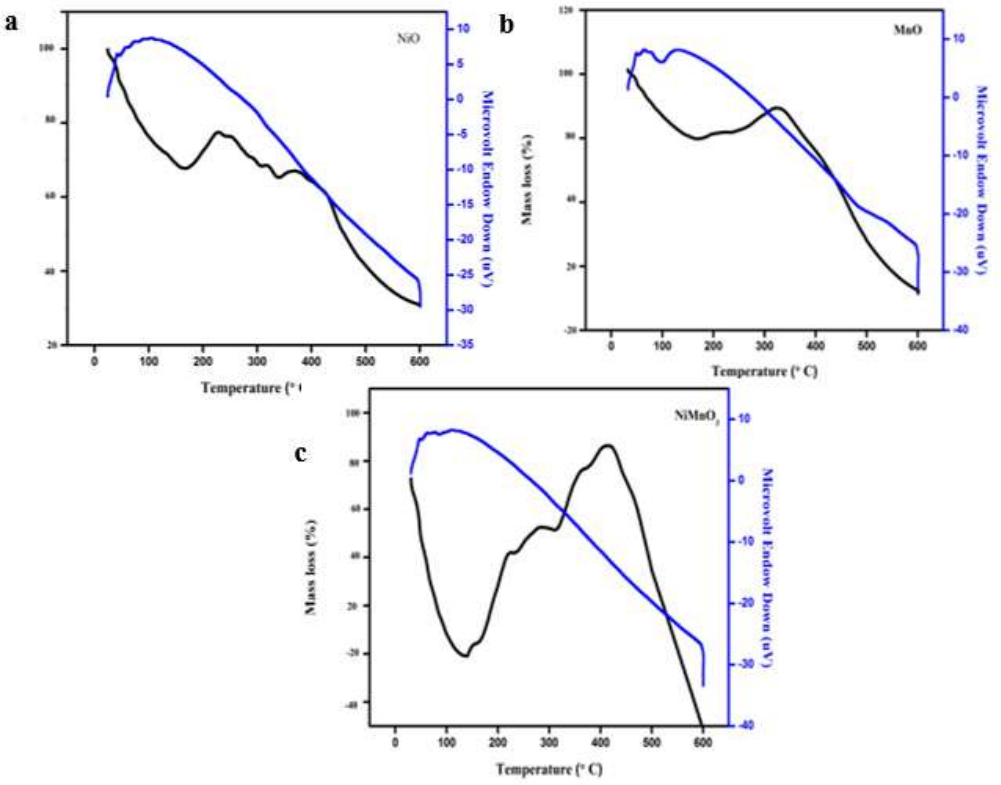

Figure 8.18 *Nano metal oxides a)NiO b) CoO c) $NiMnO_3$*

8.5.8 Powder-XRD

Figure 8.19a represents the XRD patterns of the metal oxides NiO, MnO, and $NiMnO_3$ in which the NiO exhibits the diffraction peaks at 29.35°,40.36°,65.55°,75°,80°, MnO shows peaks at 35.1°,40.2°,60.1°,70.1°,75°and $NiMnO_3$ peak arose between 29.35°,35.1°,40.2°,55.2°,65.55°, 75° where no other phases were identified in this XRD patterns and confirms the nanostructured metal oxide particles. The sharp peaks denote the purity of the target oxides and the crystallite size was calculated by Debye-Scherer [12] equation.

$$D = \frac{k\lambda}{\beta Cos\theta}$$

where D represents the size,

K signifies the Scherrer constant (0.98),

λ designates the wavelength (1.54),

β signifies the full width at half maximum (FWHM).

The current XRD patterns were matched with the JCPDS for NiO (JCPDS No. 04-0835), MnO (78-0424), and $NiMnO_3$ (75-2089) which confirms the formation of metal oxides. The structural information was linked with the data sheet obtained from the DFT framework **(Figure 8.19b)** and good agreement was realized with the current XRD patterns and it substantiates the array of metal oxide formation[13]. Lattice and physical parameters are exposed in **(Table 8.12).**

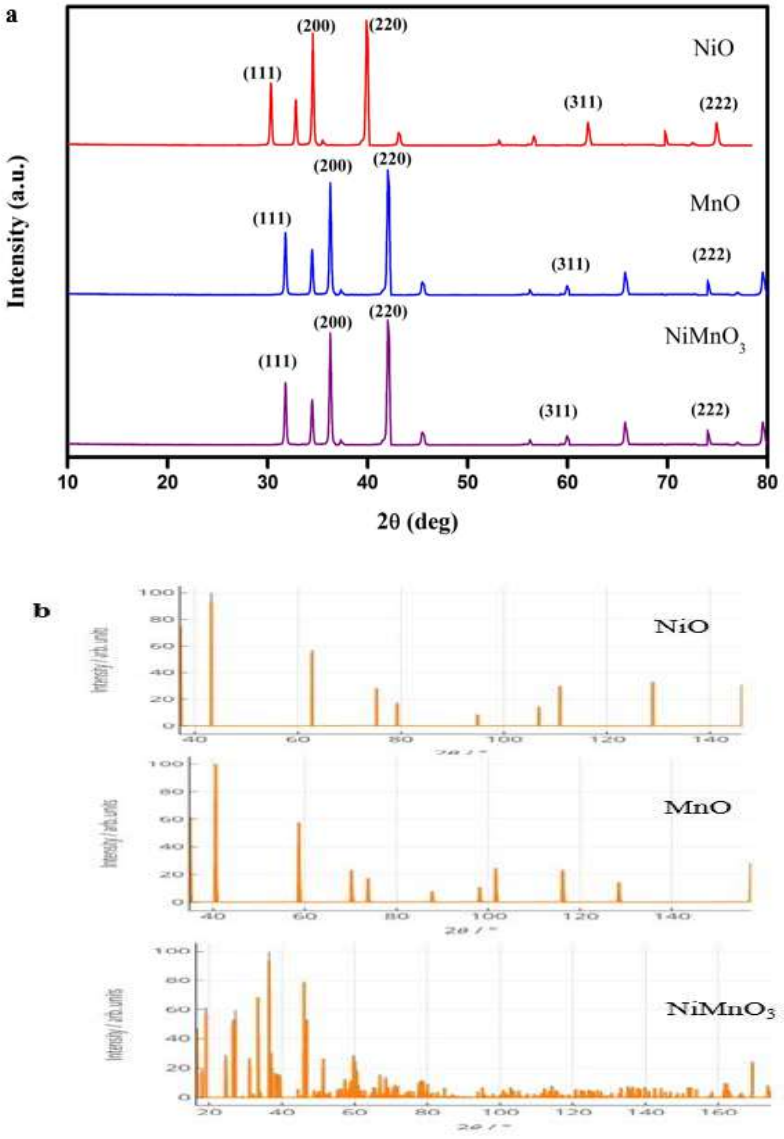

Figure 8.19 a*) X-ray diffraction patterns of metal oxides NiO, MnO, and $NiMnO_3$ b) DFT structural framework.*

Table 8.12 *Lattice parameters of nanometal oxides derived from the DFT framework*				
Metal Oxide		**MnO**	**NiO**	**$NiMnO_3$**
Lattice Parameter	**a**	4.45 Å	4.19 Å	3.95Å
	b	4.45Å	4.19 Å	5.69 Å
	c	4.45Å	4.19Å	6.11Å
Band gap (eV)		0.18	2.13	0.01
	α	90.00	90.00	104.39
Band Angle	**β**	90.00	90.00	107.70
	γ	90.00	90.00	109.80
Density		5.35 g/cm^3	6.76 /cm^3	4.74 /cm^3

8.5.9 SEM & EDAX Analyses

SEM image **(Figure 8.20a)** exhibits the appearance of coarse surface texture with multiple orifices of different patterns, as far as native mixed metal oxide $NiMnO_3$ is concerned. However, examination of the loaded metal oxide (**Figure 8.20b**) mixture reveals a smooth pattern with pores being uniformly covered, thus supporting that Pb (II) sorption had occurred. **Figure 8.20c & d** represent the variation of EDAX peaks of natant and laden $NiMnO_3$ mixture, concerning the appearance of prominent peaks at 10.5 & 7 KeV about intense Pb(II) adsorption, which occurred on the surface of the mixed metal oxide [14].

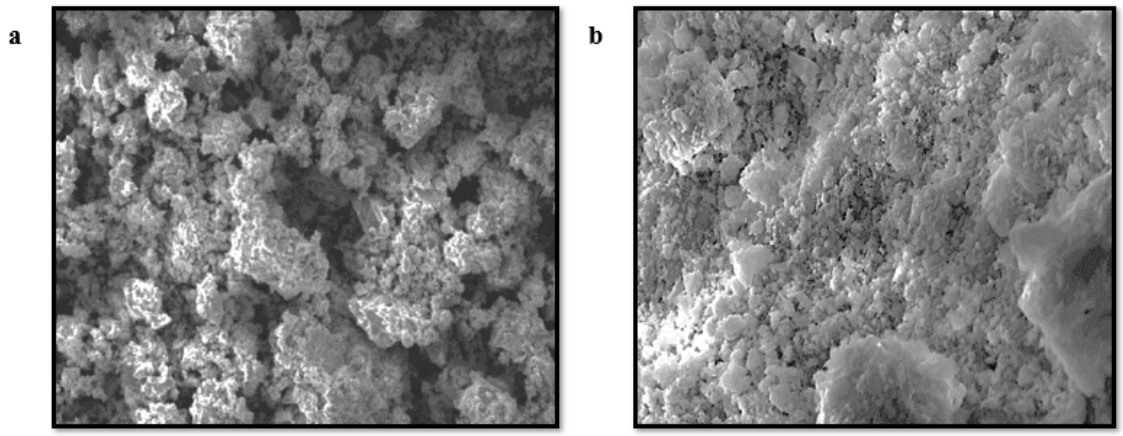

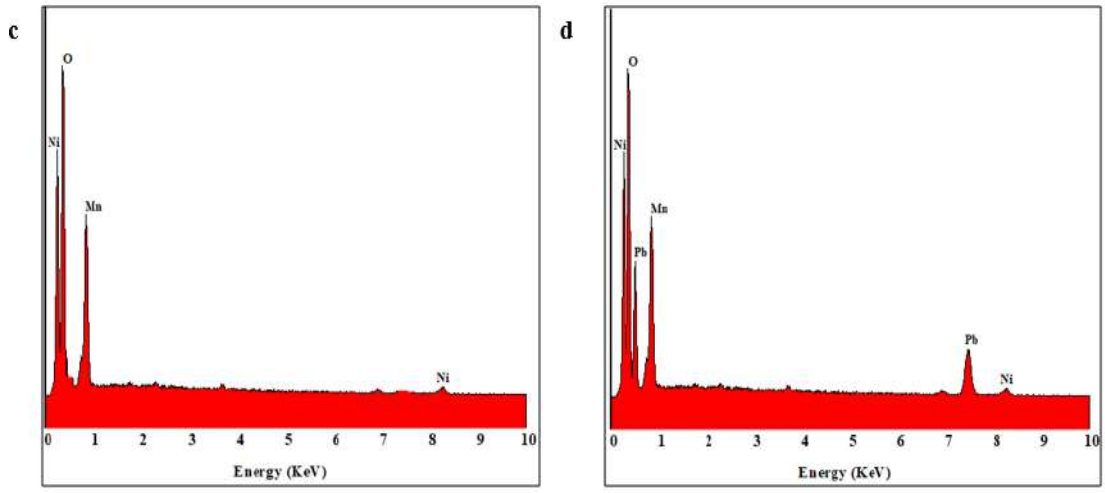

Figure 8.20 *a) Native $NiMnO_3$ mixture and b) Pb (II)- $NiMnO_3$ mixture c) Native $NiMnO_3$ mixture and d) Pb (II) – $NiMnO_3$ mixture.*

8.5.10 Effect of Initial Concentration, Adsorbent Dosage, and Contact Time

Batch experimental results show that maximum Pb (II) removal (~97%) had occurred from prepared laboratory solutions with 6 mg/L initial Pb(II) concentration and 50 mg dosage at an agitation period of 30 minutes for $NiMnO_3$ mixture against other tested metal oxides. The above statement holds good which was evident from **Figures 8.21 (a-d).**

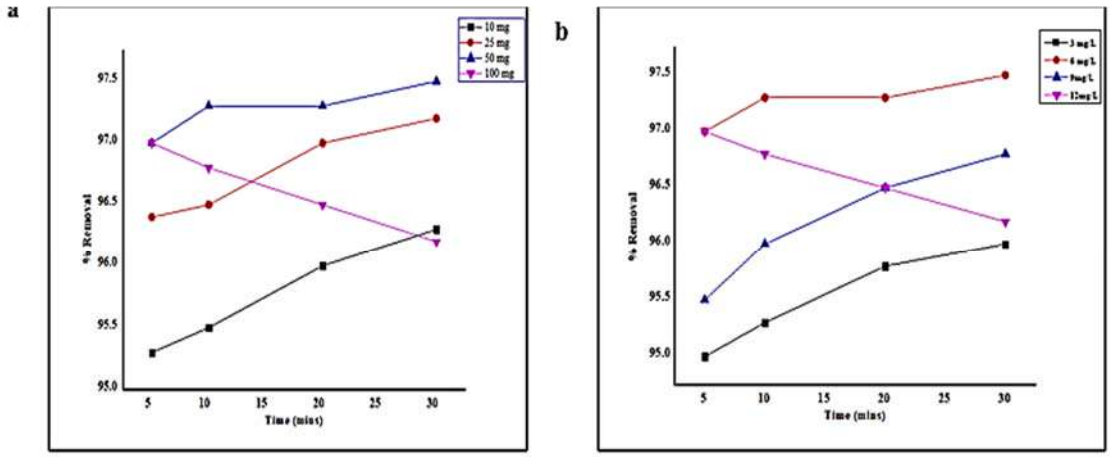

Figure 8.21 *a) Impact of Dosage and Time – $NiMnO_3$ b) Impact of Initial Concentration - $NiMnO_3$*

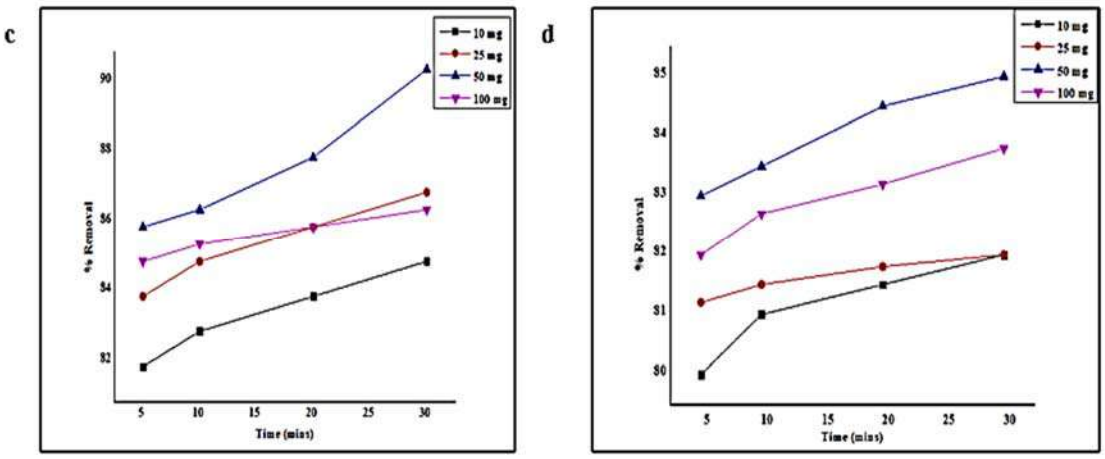

Figure 8.21 *c) Impact of Dosage – NiO d) Impact of Dosage – MnO.*

The order of preferred oxide and percentage removal of Pb^{2+} is stated as follows**:**

$NiMnO_3$ (97%) > NiO (90%) > MnO (84%)

The reason for preferred adsorption upon $NiMnO_3$ mixture shall be due to the occurrence of an enhanced amount of surface-active sites caused by the functionalization of oxide mixtures [15].

In other words, the second level priority of NiO showing a better sorptive nature than MnO shall be justified with the hydrated ionic radius parameter [16]. The lower hydrated ionic radius value (0.40 nm) for Ni^{2+} exhibits lesser hydrating capacity, thus facilitating the greater uptake of the sorbate ions against Mn^{2+}, the hydrated ionic radius (0.44 nm) of which represents its better hydrating capability than Ni^{2+}. This suffices its lesser availability to chelate Pb (II) ions.

The color intensities of solutions expressed in **Figures 8.22(a-c)** show a progressive decrease in the color of the tested laboratory sample. This experimental observation is in support of the derived results.

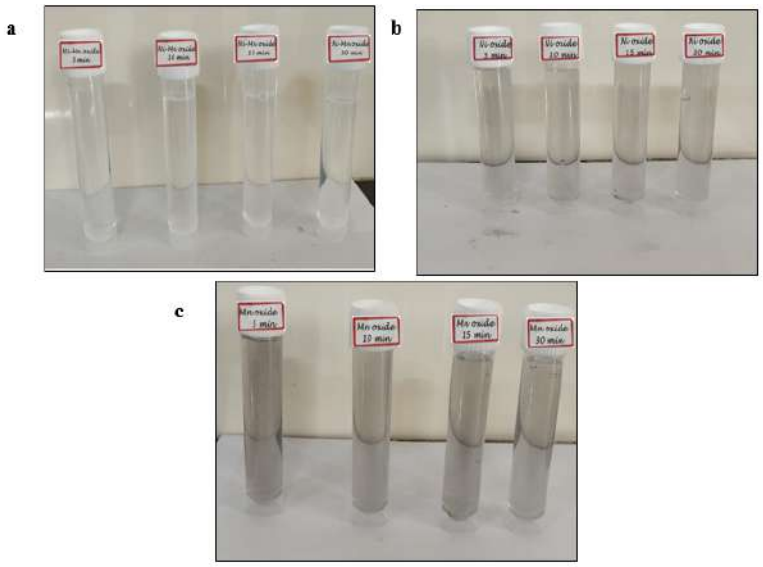

Figure 8.22 Sorption *Ability* a) $NiMnO_3$ b) *NiO* c) *MnO*

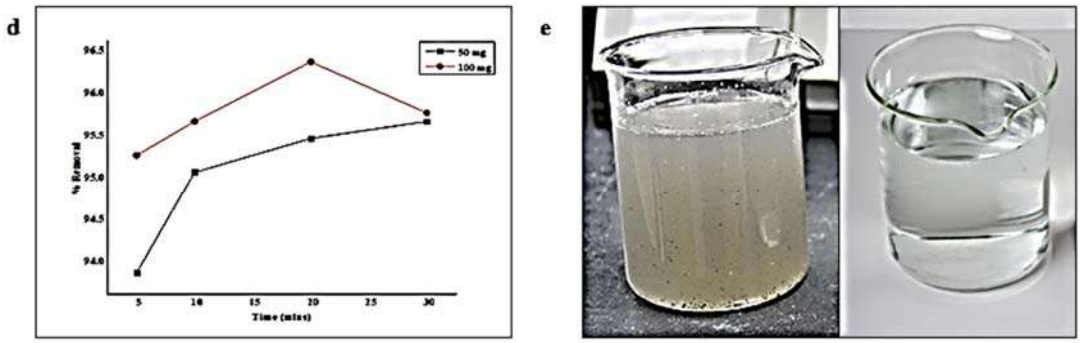

Figure 8.22 d) *Impact of Mixed Metal Oxide on Effluent e) Pictorial image of effluent & treated sample.*

The influence of the $NiMnO_3$ mixture in the deletion of Pb (II) ions from the diluted textile effluent sample (8 mg/L) is depicted in **Figure 8d**. An inclination of the curve (96% Pb (II) removal) at 20 minutes is observed for 100 mg dosage. This explains that twice the amount of dose (100 mg) is required for the field sample against the laboratory sample (50 mg). The effluent sample and the collected column eluent as a clear solution are shown in respective beakers **(Figure 8e).** The residual Pb (II) concentration of the clear solution was analyzed using AAS, thereby registering 98% Pb (II) removal with 5g dosage at the flow rate of 50 mL/ 5 min.

8.6 CONCLUSION

The derived metal complexes with 1-naphthoic acid and guanidine were categorized by CHNS analysis, TG-TA analysis, and P-XRD analysis. The spectral studies deliberate the coordination of ligands with metal ions through oxygen and nitrogen. The formation of nanoparticles was confirmed by the stretching frequency of M-O. Electronic spectral complexes revealed that all the complexes possess octahedral geometry. The optical band gap (Eg) values for metal complexes were found to be 3.2-4.6 eV. The average crystalline sizes were found to be in the range of 29-36 nm. Cu (II) metal complexes illustrate better antimicrobial activity against *Escherichia coli* than the other microbes and show more antioxidant activity.

The application towards metal complexes as an electrocatalyst with high activity in HER. The final product formed from thermal degradation was metal oxides. The redox nature of the electrocatalysts ranged from −0.15 to +2.0 V vs. RHE. It exhibits a reversible oxidation−reduction peak. Cu (II) LSV produces 98 mV and current density -3.0 V vs. RHE, respectively. The DFT data exposes an apparent synergistic effect on the compound, creating activated complexes and promoting electron allocation in hydrogen evolution.

Furthermore, the metal oxide prepared from complexes was found to be an efficient inhibitor for the treatment of wastewater effluents from industries. Further, in this study, a series of NiO, MnO, and Ni-MnO_3 oxides was confirmed by the stretching frequency of M-O. The optical band gap (Eg) values for the nano metal oxides of NiO, MnO, and $NiMnO_3$ range from 0.1-2.30 eV. The theoretical DFT band gap energy was correlated with the UV band gap energy value. XRD patterns of metal oxide were matched well with the JCPDS and DFT structural framework thereby substantiating nano metal oxide formation. Environmental application of synthesized metal oxides has been remarkably registered as pronounced sorbents for sequestrating the toxic Pb(II) ions from aqueous media by Batch mode registered 97% sequestering ability. Further extension through upscaling the lab result to field samples to Batch (96%) and column method (98%), prove the promising sorption nature of the mixed metal oxides.

REFERENCES

1. Arunadevi, N. & Vairam, S. 3-hydroxy-2-naphthoate complexes of transition metals with hydrazine-preparation, spectroscopic and thermal studies. *E-Journal Chem.* **6**, (2009).
2. Miar, M., Shiroudi, A., Pourshamsian, K., Oliaey, A. R. & Hatamjafari, F. Theoretical investigations on the HOMO–LUMO gap and global reactivity descriptor studies, natural bond orbital, and nucleus-independent chemical shifts analyses of 3-phenylbenzo[d]thiazole-2(3H)-imine and its para-substituted derivatives: Solvent and subs. *Exp. Mol. Pathol.* **45**, 147–158 (2020).
3. Ramadoss, R. & Subramania, D. Adsorption of Chromium Using Blue Green Algae-Modeling and Application of Various Isotherms. *Int. J. Chem. Technol.* **10**, 1–22 (2017).
4. Al-Zawahreh, K., Barral, M. T., Al-Degs, Y. & Paradelo, R. Competitive removal of textile dyes from solution by pine bark-compost in batch and fixed bed column experiments. *Environ. Technol. Innov.* **27**, 102421 (2022).
5. Palma-Anaya, E. *et al.* Pb(II) removal process in a packed column system with xanthation-modified deoiled allspice husk. *J. Chem.* **2017**, (2017).
6. Adamu, C. A., Bell, P. F., Mulchi, C. & Chaney, R. Residual metal concentrations in soils and leaf accumulations in tobacco a decade following farmland application of municipal sludge. *Environ. Pollut.* **56**, 113–126 (1989).
7. Khairnar, S. D. & Shrivastava, V. S. Facile synthesis of nickel oxide nanoparticles for the degradation of Methylene blue and Rhodamine B dye: a comparative study. *J. Taibah Univ. Sci.* **13**, 1108–1118 (2019).
8. Swathika, M. & Natarajan, A. Synthesis and photometric properties of efficient white-emitting phosphor of M-AMG transition metal complexes for OLED applications. *Luminescence* (2022).
9. Cinthia, A. J., Rajeswarapalanichamy, R. & Iyakutti, K. First principles study of electronic structure, magnetic, and mechanical properties of transition metal monoxides TMO(TM=Co and Ni). *Zeitschrift fur Naturforsch. - Sect. A J. Phys. Sci.* **70**, 797–804 (2015).

10. Chen, H. *et al.* Revealing the Relationship between Energy Level and Gas Sensing Performance in Heteroatom-Doped Semiconducting Nanostructures. *ACS Appl. Mater. Interfaces* **10**, 29795–29804 (2018).
11. Teo, S. H., Rashid, U. & Taufiq-Yap, Y. H. Heterogeneous catalysis of transesterification of jatropha curcas oil over calcium-cerium bimetallic oxide catalyst. *RSC Adv.* **4**, 48836–48847 (2014).
12. Shen, Y. & Lua, A. C. Sol-gel synthesis of Ni and Ni supported catalysts for hydrogen production by methane decomposition. *RSC Adv.* **4**, 42159–42167 (2014).
13. Hegde, G. S., Prabhu, A. N., Rao, A., Gurukrishna, K. & Deepika Shanubhogue, U. Investigation of near-room and high-temperature thermoelectric properties of (Bi0.98In0.02)2Se2.7Te0.3/Bi2Te3 composite system. *J. Mater. Sci. Mater. Electron.* **33**, 25163–25173 (2022).
14. Hasan, R. & Setiabudi, H. D. Removal of Pb(II) from aqueous solution using KCC-1: Optimization by response surface methodology (RSM). *J. King Saud Univ. - Sci.* **31**, 1182–1188 (2019).
15. Pan, Y., Shen, X., Yao, L., Bentalib, A. & Peng, Z. Active Sites in Heterogeneous Catalytic Reaction on Metal and Metal Oxide: Theory and Practice. *Catal. 2018, Vol. 8, Page 478* **8**, 478 (2018).
16. Mähler, J. & Persson, I. A study of the hydration of the alkali metal ions in aqueous solution. *Inorg. Chem.* **51**, 425–438 (2012).
17. Alhalili, Z. Metal Oxides Nanoparticles: General Structural Description, Chemical, Physical, and Biological Synthesis Methods, Role in Pesticides and Heavy Metal Removal through Wastewater Treatment. *Mol. 2023, Vol. 28, Page 3086* **28**, 3086 (2023).